Radiation-enhanced fission track annealing revisited and consequences for apatite thermochronometry

Kalin T. McDannell [1*], Dale R. Issler [1], and Paul B. O'Sullivan [2]

[1]*Geological Survey of Canada, Natural Resources Canada, 3303 33 St. NW, Calgary, AB, T2L 2A7 Canada*

[2]*GeoSep Services, 1521 Pine Cone Rd., Moscow, ID, 83843 United States*

[*]Corresponding author: kalin.mcdannell@canada.ca

ABSTRACT

Apatite fission track (AFT) analyses for granitoid and metamorphic bedrock samples from the Western Superior Province (Ontario), the Churchill-Rae Province (Melville Peninsula and Southampton Island, Nunavut), and the Slave Province (Northwest Territories) show a broad range of single grain effective uranium concentrations (eU) (<1 to ~300 ppm) and some of the oldest reported AFT ages in North America. Although most of our samples are characterized by near-endmember fluorapatite composition with implied low track retentivity (<0.1 apfu Cl, r_{mr0} ~0.85-0.82), single-grain AFT ages are statistically overdispersed and ages decrease with increasing eU content. This eU-age relationship is resonant of the Hendriks and Redfield (2005) *Earth Planet. Sci. Lett.* **236** (443-458) argument for α-radiation enhanced fission track annealing (REA) and is analogous to the negative age-eU correlations observed in published zircon and titanite (U-Th)/He data from slowly-cooled cratonic rocks. In all cases, the samples fail the canonical χ^2 test (<5%), generally considered to indicate that the ages are unlikely to be drawn from a single Poissonian distribution with a discrete mean value and may represent multiple populations. The high intra-sample age variability for low-Cl bedrock apatites with protracted histories (>200-500 m.y.) at <100°C since the Precambrian suggests strong REA control on AFT ages. Conversely, some low Cl AFT samples with a narrower eU range show less age dispersion and a weak apparent age-eU correlation. A complex trade-off between radiation damage, chemical composition (e.g. low Cl and REE enrichment), and thermal history is implied when eU and r_{mr0} are positively correlated. Previous assessments of the influence of REA on AFT age were based on evaluating central age and mean track length, which potentially mask high single-grain age scatter and REA effects due to the modal nature of central age determination. REA is also supported by and compatible with materials science and nuclear waste studies of radiation damage in different apatite groups, therefore it is crucial that bedrock samples exhibiting high age scatter are evaluated in terms of intra-sample compositional heterogeneity. AFT samples with relatively low Cl concentrations are especially prone to greater REA control of cooling ages and this underscores the need for routine acquisition of compositional data for AFT datasets. Our broad range in single-grain AFT ages (with no other clear, strong compositional controls) supports the notion that radiation damage affects both the AFT and (U-Th)/He thermochronometers in slowly-cooled settings and must be accounted for during thermal history modeling and interpretation.

Keywords: apatite; fission track; alpha damage; radiation-enhanced annealing; uranium

1. Introduction

Uranium and thorium-rich minerals accumulate radiation damage over geological time, with the primary spontaneous decay process in apatite being ^{4}He α-particle emission during ^{238}U decay (Donelick et al., 2005 for review). The majority of radiation damage results from α-recoil in the apatite lattice, whereas fission events are a minor contribution (for every ~2 million ^{238}U nuclei undergoing α-decay only one fission event occurs, e.g. Donelick et al., 2005). The ion-spike explosion model of Fleischer et al. (1965) states that positive ions created by the transmission of highly charged fission fragments repel one another and form a cylindrical region of crystal damage. The fission track dating method is based on the accumulation of these crystallographic damage trails due to spontaneous nuclear fission in U-bearing minerals such as apatite $Ca_5(PO_4)_3(OH,F,Cl)$ (Price and Walker, 1963; Wagner, 1968; Naeser and Faul, 1969). Apatite fission track (AFT) thermochronology is established on the principle that crystal damage from fission fragments is annealed with increasing temperature, which results in a quantifiable reduction to track lengths and track density in the apatite volume (e.g. Gleadow and Duddy, 1981; Green, 1988). However, difficulties remain in fully characterizing the thermally-activated annealing behaviour of fission tracks at geologic timescales and the temperature of complete track annealing, as these factors are influenced by duration of heating (Duddy et al., 1988; Green et al., 1986; Green, 1988; Green et al., 1989), variable apatite composition (i.e. common fluorapatite vs. chlorapatite; Carlson, 1990; Barbarand et al., 2003; Carlson et al., 1999), and crystal anisotropy (e.g. Donelick et al., 1999; Ketcham et al., 2007; Nadzri et al., 2017). Chlorine content is considered the dominant compositional control (Green et al., 1986) on fission-track retentivity when >0.1 atom per formula unit, apfu or >0.35 wt.% (Barbarand et al., 2003), along with secondary Ca-site (substituting) cations, such as Fe, Na, Mn, Sr, and Mg, and some rare-earth elements (REE) such as La and Ce (Barbarand et al., 2003; Carlson et al., 1999; Ravenhurst et al., 2003). However, the trade-offs between kinetic variability, elemental substitutions, and track annealing behaviour are multifaceted and not fully understood (Barbarand et al., 2003; Ketcham et al., 1999; Ketcham et al., 2007).

The internal structure of fission tracks in apatite control the annealing process, which is very different from zircon annealing where amorphous tracks “heal” by recombination of vacancies and interstitials in the track interior (Li et al., 2010; Li et al., 2011; Li et al., 2012). Track

shortening in apatite occurs due to thermo-emission of vacancies from the porous track core to the adjacent crystalline matrix (Li et al., 2010; Li et al., 2011) and tracks become discontinuous or segmented due to Rayleigh instability, Brownian motion, or motion of track segments due to the high surface energy and diffusivity of voids (Li et al., 2011). To complicate annealing behaviour further, it has been well known for decades that there are small length differences between spontaneous and induced tracks and that apatite FT annealing of up to 10-15% or ~1.5-2.5 μm (fading) can occur at ambient temperatures over millions to billions of years (e.g. Crowley et al. 1991; Donelick et al., 1990).

In contrast to fission events, α-decay damage accumulates in minerals through energetic α-particle exchange by ionization and electronic excitation and by α-recoil "ballistic" collisions with atomic nuclei in the mineral lattice (e.g. Ewing and Weber, 2010; Weber et al., 2015). The α-recoil collisions produce more damage due to the greater destructive interaction with the crystal structure (Holland and Gottfried, 1955). The accumulation of energetic particles in the crystal and a high-energy absorption rate can result in self-heating from α-decay and permanent structural defects can form as a result of energetic electron interactions, which produce electron-hole pairs – resulting in charged defects, bond rupture, and increased defect diffusion in fluorapatite (Ewing and Weber, 2010; Wang et al., 1994). Damage results in the formation of point defects and defect clustering within the mineral lattice and causes a crystalline-to-amorphous transition at high levels of damage (e.g. Ewing et al., 2000; Ewing and Weber, 2010; Weber et al., 2012). The primary α-radiation damage mechanisms include the "direct impact" and "defect accumulation" models (Ewing et al., 2000 and refs. therein). The direct impact model (e.g. Gibbons 1972; Morehead and Crowder, 1972) is predicated on the assumption that an amorphous (non-crystalline) region is formed within the core of a displacement cascade, and complete amorphization is reached when the amorphous domains increase with ion dose, eventually occupying the entire sample. The point defect accumulation model (e.g. Gibbons 1972; Jackson 1988) assumes that emitted particles create discrete point defects and that amorphization is achieved when the local defect concentration reaches a critical level. For example, the α-decay of U and Th in natural apatites containing REE and Si leads to a crystalline-to-amorphous "metamict" change due to radiation damage accumulation – contingent

upon composition, crystalline structure, irradiation level, and temperature (Weber et al., 1997). The general view is that at low temperatures, typical phosphate apatite compositions require less radiation to become amorphized than silicate apatites (e.g. Wang et al., 1994; Weber et al., 1997). Durango fluorapatite ($Ca_{10}(PO_4)_6F_2$) becomes amorphized at lower temperatures and at lower radiation dose than silicate-apatite ($Ca_2La_8(SiO_4)_6O_2$), however at temperatures ≥77°C, fluorapatite required 5x higher dose to become amorphous than silicate apatite (Wang et al., 1994). The critical temperature for amorphization varies depending on the irradiation dose (Ewing et al., 2000), however apatite composition and temperature directly play a role in the persistence of α-radiation damage and the example of increased silica content shows a reduction in the recrystallization tendency of apatite (Ewing et al., 2000). This raises the question of whether and how (other) unusual elemental substitutions known to affect apatite retentivity (e.g. Carlson et al., 1999; Gautheron et al., 2013; Djimbi et al., 2015; Ravenhurst et al., 2003) coupled with slow cooling (≤1-3°C) and minor, episodic thermal annealing events over billion year timescales play a role in modulating bulk radiation damage accumulation, annealing, and recrystallization in apatite.

Radiation damage has implications for multiple diffusion-based thermochronometers, and even though fission track dating is established on constraining crystalline damage, the suspected effects of α-damage on track annealing have been controversial (e.g. Hendriks and Redfield, 2005). A drawback of fission-track dating with respect to visualizing damage is that the process of increasing the optical visibility of tracks requires chemical etching, which erases the initial damage structure and essential information about the physical scale of radiation damage (Afra et al., 2011). Ion tracks are similar in character to fission tracks (Rabone et al., 2008) and ion track annealing experiments from swift heavy ion bombardment in apatite verify unit-cell increases during irradiation, crystal strain and cracking at high ion fluence, high-pressure reduction of amorphization, radiation-enhanced diffusion, and anisotropic lattice damage response (e.g. Liu et al., 2008; Miro et al., 2005; Miro et al., 2012; Weikusat et al., 2011). Latent ion particle tracks in Durango apatite were found to anneal via a two-stage process of structural relaxation followed by recrystallization (Afra et al., 2011), which has also been observed in silicate apatite (Bae et al., 2007). Ionization-annealing of ballistic damage in SiC revealed a surprisingly low threshold

for electronic energy loss (a few MeVs) to initiate annealing at room temperature and repair defect clusters, crystalline structure, and displacements at the atomic level (Zhang et al., 2015). Carpéna (1998) proposed that annealing in low-temperature conditions is also possible for silicate apatite (fluorbritholite) with lanthanide enrichment (e.g. La, Ce) or cation substitutions such as Na, Mg, Sr, Mn, Fe, U, and Th.

Radiation damage is often discussed in terms of "alpha dose," which is a quantitative estimate of the self-irradiation (driven by the α-fluence) in a mineral from time-integrated damage accumulation (e.g. Nasdala et al., 2001). The first-order control on α-damage is U content, or "effective U" concentration (eU=U+0.235×Th+0.0046×Sm; Gastil et al., 1967) of the host grain weighted for parent α-productivity. Extreme α-damage levels cause crystallographic amorphization in zircon due to relatively high U content (Chakoumakos et al., 1987; Murakami et al., 1991; Nasdala et al., 2001), whereas α-damage is more easily recoverable in apatite (Weber et al., 1997; Li et al., 2017). (U-Th)/He dating of zircon is an excellent example of a mineral demonstrating a relationship between diffusivity and α-dose/eU. The expectation is that a positive age-eU correlation exists at low dose and a negative relationship is evident after the damage percolation threshold (or point at which damage interconnects) is reached, causing increased diffusivity (Guenthner et al., 2013). There is an expected decrease in ^{4}He diffusivity at the α-recoil percolation dose of ~2.5-3.1×10^{16} α/g and then an increase in diffusivity at fission track percolation achieved at a higher damage level of ~1.9×10^{18} α/g (Ketcham et al., 2013). The zircon radiation damage and accumulation model (ZRDAAM; Guenthner et al., 2013) predicts a complex diffusive relationship between damage accumulation/annealing (eU) and derived He age that is strongly influenced by thermal history. Self-irradiation over geological timescales results in high α-doses above the percolation point and a negative age-eU relationship should become apparent in grains that have accumulated high radiation damage and spent significant time below the He partial retention zone. This age-eU pattern is achieved either through He loss at low temperatures or alternatively, rocks spending considerable time at low temperatures and experiencing a thermal pulse during their history (Guenthner et al., 2013). The model for zircon radiation damage has been recently improved upon to show that bulk radiation damage annealing requires longer durations and higher temperatures than fission track annealing, and when fission

tracks are fully annealed, the total radiation damage has only been annealed ~30-50% (Ginster et al., 2019). Fission track annealing characteristics between zircon and apatite are different (Li et al., 2011), but α-recoil damage is known to diminish fission track thermal stability in U-bearing phases such as zircon (Garver et al., 2004; Kasuya and Naeser, 1988), titanite (Lumpkin et al., 1991), and apatite (Carpéna and Lacout, 2010; Ritter and Märk, 1986). These findings imply that the presence of α-damage lowers the stability of fission tracks in minerals commonly used in thermochronology and that α-damage can persist above temperatures typically believed to completely anneal fission damage.

The apatite (U-Th)/He (AHe) thermochronometer is affected by radiation damage (e.g. Shuster et al., 2006; Shuster and Farley, 2009). There are consequences for He diffusion in a damaged mineral lattice, with the main assertion being that radiation-induced damage impedes helium diffusivity and that damage evolves as a function of temperature and eU concentration (e.g. Farley, 2000; Flowers et al., 2009; Gautheron et al., 2009; Ketcham et al., 2017; Recanati et al., 2017; Shuster et al., 2006; Shuster and Farley, 2009). Radiation damage effects on He retentivity have been explored and described through models of diffusive loss (Shuster et al., 2006; Flowers et al., 2009; Gautheron et al., 2009; Gerin et al., 2017; Willett et al., 2017). There is now a better understanding of the numerous factors affecting He diffusivity in apatite including compositional and crystallographic controls on α-damage annealing (Djimbi et al., 2015; Gautheron et al., 2013; Gautheron et al., 2009), crystallographic microvoids (Zeitler et al., 2017), vacancy damage (Gerin et al., 2017), and strain-induced dislocation traps (McDannell et al., 2018b). The α-damage recoil track percolation threshold has been recently described for He diffusivity in apatite (Ketcham et al., 2017; Recanati et al., 2017), and seems genetically similar to damage modes in zircon. A similar age-α-dose relationship has been observed for titanite (Baughman et al., 2017; Guenthner et al., 2017), however a titanite radiation damage model has yet to be formally described. Due to the difficulty in direct damage observation in past studies and in determining α-recoil kinetics, α-damage annealing in apatite has long been considered analogous to fission track annealing behaviour, and the most commonly used empirical diffusion models of damage accumulation and annealing are established on this principle (Flowers et al., 2009; Gautheron et al., 2009). However, it has been previously proposed that the rate of α-damage annealing is slower than fission-track annealing (e.g. Ritter and Märk, 1986), which would

192 require revision of existing models. The dilemma is that we really do not know what the kinetics
193 are for α-damage annealing, and most importantly in this context, we should not assume that it is
194 the same for both damage types. We have done so for the purposes of trying to model damage
195 effects on He diffusion in apatite, but with arguably limited success especially in geologic
196 settings where the kinetics for each damage mode diverge.
197
198 The developments in understanding how α-damage acts to modify He diffusion are integral for
199 using apatite as a viable thermochronometer and undoubtedly have implications for AFT analysis
200 and fission-track retention in rocks that have experienced slowly-cooled histories. The relatively
201 subtle kinetic and compositional controls on apatite annealing and retentivity in rapidly-cooled
202 settings become more complex and magnified in cratonic interiors due to their protracted thermal
203 histories at low temperatures (e.g. Green and Duddy, 2006; Flowers, 2009). There have been
204 many problems associated with the interpretation of both AFT and AHe data in slowly-cooled
205 settings, including significant intra- and inter-sample age dispersion (e.g. Fitzgerald et al., 2006;
206 McKeon, 2012; McDannell et al., 2018b) and AFT<AHe cooling age inversion (e.g. Hendriks
207 and Redfield, 2005; Green et al., 2006; Flowers and Kelley, 2011). Hendriks and Redfield (2005)
208 suggested that elevated U concentration in apatite has a strong influence on fission-track
209 annealing, invalidating prior thermochronologic interpretations for cooling signals across the
210 Fennoscandian Shield. In a series of papers, this matter and the robustness of AFT versus AHe
211 dating was debated (Green and Duddy, 2006; Hendriks and Redfield, 2006; Larson et al., 2006).
212 Hendriks and Redfield's argument for AHe dates being more reliable than AFT ages was
213 contested and attributed to variability in He retentivity, rather than variability in AFT annealing
214 behaviour (Green et al., 2006). The apparent U control on AFT ages was instead attributed to
215 lithologic differences and elevated Cl content for the analysed apatites (Kohn et al., 2009).
216
217 The effect of U on AFT ages was perhaps dismissed prematurely, and analytical advances in the
218 past 15 years have motivated changes in AFT methodology to better address this problem. The
219 potential relationship between U and AFT age has long been recognized and an early example of
220 a negative correlation between zircon FT age and U concentration was given in Carter (1990)
221 using the external detector method (EDM). Discussion around this relationship focused on

single-grain U variability, track density, and potential counting biases, as well as the fact that both AFT age and U estimates are derived from the same induced track count, and therefore related. The recommendation in Carter (1990) for determining if a real association exists between age and U is to measure U independently. The introduction of laser ablation inductively coupled plasma mass spectrometry (LA-ICP-MS) for AFT dating (Hasebe et al., 2004) made the direct measurement of U procedurally advantageous over the EDM, which uses an irradiated, low-U muscovite detector as a proxy for apatite ^{238}U content through reactor-induced fission. The main drawback for ICP-MS ^{238}U measurement is that very low U content (<< 0.5 ppm) is difficult to measure and leads to modestly older ages compared to the EDM (Seiler et al., 2013), nonetheless U can still be reliably measured at <1 ppm. It is also well established that apatites with high fission-track density (i.e. old grains or high U) are more difficult to measure using the EDM, consequently biasing AFT measurements towards younger or low U grains (e.g. Carter, 1990; Seiler et al., 2013). In a series of analyses on laboratory age standard AFT grains, Hasebe et al. (2004) showed that the EDM underestimated the U content of high U, whole-grain laboratory age standard apatites with respect to LA-ICP-MS measurements.

In light of advances in precise, *in situ* U concentration measurements for AFT analysis, re-evaluation of α-radiation enhanced annealing (REA) is warranted. Assessing the viability of REA in slowly-cooled terranes is important for the understanding of the annealing kinetics of apatite fission tracks and the implications for other thermochronometers that are affected by the same α-damage and annealing processes, such as the case with the apatite (U-Th)/He system (Gautheron et al., 2013; Gautheron et al., 2009; Recanati et al., 2017; Shuster et al., 2006). We present new LA-ICP-MS AFT data from Archean-Paleoproterozoic plutonic granitoids and gneissic bedrock samples from localities across the Canadian Shield and assess the REA potential related to U content. In general, grains that are characterized by highly variable eU and low Cl concentrations (<0.1 apfu) typically show a strong, negative age-eU correlation, whereas contrasting metasedimentary samples from southern Baffin Island with "typical apatite" eU levels (less variability, ~20-30 ppm) and low Cl (<0.1 apfu) show seemingly weak U control on age, less single-grain age scatter, or display complex relationships between retentivity proxies (i.e. eU and r_{mr0}).

253 Our intent is not aimed at generating a calibrated model of REA behaviour, nor wholly
254 reconciling observations between AFT and AHe single-grain ages in slowly-cooled settings for
255 geologic interpretation – but rather to bring REA back into the communal foreground and assert
256 that this phenomenon exists, although it is poorly understood due to complexities associated with
257 fission-track annealing.
258

259 **2. Regional Geologic Setting**

260 The AFT samples presented here all come from exposed Precambrian granitic and gneissic
261 bedrock across Canada. An overview of the Precambrian geologic history of the Canadian Shield
262 is provided by Hoffman et al. (1989) and here we focus mainly on areas of Archean (>2.5 Ga)
263 crust that are currently exposed across the Canadian interior that were sutured during Trans-
264 Hudson orogenesis and Laurentia assembly at ca. 1.9-1.8 Ga. The major terranes that were
265 sampled are the Western Superior Province (Percival et al., 2012), rocks of the northeastern
266 Churchill Province-Rae domain at Southampton Island (Berman et al., 2013) and Melville
267 Peninsula (Berman et al., 2015), and the Slave Province (Isachsen and Bowring, 1994) all shown
268 on figure 1. Results from southern Baffin Island are also shown for comparison to the
269 aforementioned data (see discussion).

270 The Archean-Proterozoic tectonomorphic history and setting for each terrane is thoroughly
271 described in their respective reference. All of these regions have presumably been exposed at
272 near surface conditions or in the upper crust since the late Proterozoic and experienced minor,
273 episodic burial throughout the Phanerozoic (Burgess, 2008; Miall and Blakey, 2008). The
274 Archean-Paleoproterozoic age of these terranes and the limited Phanerozoic sedimentary strata
275 provide few constraints on the burial and exhumation history of these rocks. The Phanerozoic
276 sedimentary succession in central Canada is preserved in Hudson Bay (mainly Paleozoic, ~2500
277 m thick; fig. 1) and unconformably overlies Canadian Shield bedrock (Pinet et al., 2013). The
278 Paleozoic platform sequence is exposed in the Western Superior Province at Hudson and James
279 Bay, and Ordovician-Silurian sediments onlap much of the southern Arctic, northern Melville
280 Peninsula (Corrigan et al., 2013), and Baffin Island crystalline bedrock (fig. 1).
281

In the absence of formal models for the time-temperature history of many of these areas, geologic evidence and the sparse Phanerozoic sedimentary record yield clues about the thermal history experienced by Shield rocks. Kimberlites can include sedimentary xenolith evidence of the pre-existing Paleozoic cover that was removed by erosion. The Jericho kimberlites in the central Slave craton have limestone xenoliths of Middle Devonian age (L. Eifelian-E. Givetian) (Cookenboo et al., 1998) and the ca. 75-45 Ma Lac de Gras kimberlite field suggests up to ~1.4 km of Cretaceous strata existed at that time (Nassichuk and McIntyre, 1995; Stasiuk et al., 2006). The Mesozoic Kirkland Lake (Ontario) kimberlites contain Ordovician-Devonian xenoliths in the Superior Province (McCracken et al., 2000) and the Jurassic Chidliak kimberlites of southern Baffin Island also contain Late Ordovician-Early Silurian xenoliths (Zhang and Pell, 2014). These areas all indicate that most of interior Canada was inundated by a shallow sea in the middle Paleozoic and experienced some level of regionally cohesive burial and exhumation through Paleozoic-Mesozoic time, which is reinforced by regional studies using low-temperature thermochronology (Ault et al., 2009; Ault et al., 2013; Feinstein et al., 2009; Kohn et al., 2005). AFT studies suggest that most of the Trans-Hudson region remained at <80-90°C since the Ordovician (Pinet et al. 2016) and that rocks of the Superior Province in Ontario were never hotter than ~90°C during episodic burial and exhumation since the Cambrian (Kohn et al., 2005). Generally speaking, the majority of the Canadian Shield has been at temperatures <100-120°C at least since the latest Precambrian-Cambrian (~600-500 Ma).

3. Analytical Methods

3.1 LA-ICP-MS apatite fission track analysis

AFT ages were determined using the LA-ICP-MS method (Hasebe et al. 2004; Donelick et al. 2005; Chew and Donelick 2012), which gives similar results to the traditional external detector method but avoids the requirement for sample irradiation in a nuclear reactor (e.g. Seiler et al., 2013). A single grain mount was used to acquire AFT age, length, and D_{par} data for each sample according to the procedures described in Donelick et al. (2005). Following mineral separation procedures, apatite separates were mounted in epoxy, polished, and etched in 5.5M HNO_3 for 20s at 21°C to reveal all natural fission tracks intersecting the polished grain surface. For each age grain, locations were recorded and spontaneous AFT densities were counted using a microscope at 2000x magnification under unpolarized light. ^{238}U concentrations were determined

for the track count areas on each age grain using the Washington State University (WSU) Finnigan Element II Magnetic Sector ICP-MS by measuring the weighted mean ratio of ^{238}U to ^{43}Ca from multiple spot analyses at a fixed laser point (^{232}Th and ^{147}Sm were also measured). The volume of ablated material is estimated using ^{43}Ca, assuming that Ca occurs in stoichiometric amounts. AFT ages were calculated using the LA-ICP-MS ζ-calibration approach (Donelick et al., 2005; Vermeesch, 2017) based on the Durango apatite age standard. Apatite U-Pb age data were acquired for AFT age grains as described in Chew and Donelick (2012). Apatite U-Pb age density plots were created using DensityPlotter v. 8.2 software (Vermeesch, 2012) using a Kernel Density Estimator with an adaptive bandwidth and logarithmic transformation of the single-grain common Pb-corrected isotopic sum ages and their 2σ errors. The quoted "mixture model" ages (table 1) incorporate all measured isotopic sum ages and are for a single age population.

3.2 Apatite elemental analyses and the "effective" Cl kinetic parameter

Sample apatite grains were analysed for 13 elements (F, Na, Mg, P, S, Cl, Ca, Mn, Fe, Sr, Y, La, and Ce) by electron probe microanalysis (EPMA) at the Washington State University Peter Hooper Geoanalytical Laboratory using a JEOL JXA8500F Field Emission Electron Microprobe operated at 15 kV (20 nA current) with a beam size of 5 μm. Laboratory weight % oxide values were converted to atom per formula unit (apfu) values, including estimation of OH content from Cl and F values, using the apatite stoichiometric model of Ketcham (2015). The r_{mr0} kinetic parameter was calculated for each analysed apatite grain by substituting the apfu values into the multivariate equation of Carlson et al. (1999). The nonlinear r_{mr0} values were converted into "effective" Cl (eCl) values (in apfu) using the empirical r_{mr0}-Cl relation of Ketcham et al. (1999) for better visualization of data on a linear scale, for calculating arithmetic means of single-grain kinetic parameters, and for comparison with the commonly used measured Cl kinetic parameter. D_{par} (mean etch pit diameter perpendicular to c-axis; e.g. Donelick et al., 2005) data are not discussed in detail here. However, D_{par} has been found to be a lower precision kinetic proxy when compared to r_{mr0} or measured Cl (Issler et al., 2018), and in other localities across Canada it has demonstrated limited utility in successfully separating apatite grain age populations (e.g. Issler and Grist, 2008; McDannell et al., 2019; Powell et al., 2017; Schneider and Issler, 2019). In the majority of our samples, measured Cl and D_{par} show no relation with AFT age and in

342 general, eCl is preferred as a kinetic parameter over measured Cl because it takes into account
343 the contribution of multiple elements that influence track retentivity (e.g. Barbarand et al., 2003;
344 Carlson et al., 1999). Negative eCl values ($r_{mr0} > 0.84$) indicate that AFT track retentivity is
345 lower than that of the apatite used for the laboratory annealing experiments (Ketcham et al.,
346 1999). We use the Carlson et al. (1999) r_{mr0} equation rather than the Ketcham et al. (2007)
347 equation because in our experience with multi-kinetic AFT populations the former generally
348 produces a broader range of r_{mr0} values than the latter equation for apatites displaying a range of
349 kinetic behavior. The greater spread in values can result in better discrimination between kinetic
350 age populations. Ketcham et al. (2007) demonstrates that both experimental datasets can be
351 reconciled but this does not necessarily mean that the latter equation is superior. Refitting of the
352 model parameters in the newer equation may be influenced by: (1) the narrower compositional
353 range of the Barbarand et al. (2003) experimental apatite compared with those of Carlson et al.
354 (1999), which may be biasing the fit due to the overriding influence of Cl and (2) there may be
355 residual analyst bias between experiments even after corrections were applied.

356

357 **4. Apatite fission track results**

358 We present new LA-ICP-MS AFT results for 12 samples taken from cratonic crystalline bedrock
359 across the Canadian interior (table 1; refer to the Supporting Information [SI] for all raw
360 analytical data). Two other new samples from Baffin Island are not from crystalline bedrock, but
361 are from Paleoproterozoic metasediments overlying Archean basement that have internally
362 consistent apatite U-Pb ages and are treated as homogeneous samples. The Baffin Island AFT,
363 apatite U-Pb, and EPMA datasets (McDannell et al., 2018a) are available from
364 http://dx.doi.org/10.1594/IEDA/111241. There is also an additional AFT sample with
365 accompanying AHe data previously published for the Hudson Bay region in Pinet et al. (2016)
366 that is examined in the discussion (see table 1). Published AFT data from Canada and other areas
367 worldwide are included for comparison only to illustrate other types of complex relationships
368 between AFT single-grain age, eU/α-dose, and other kinetic parameters (see discussion). We
369 want to emphasize that this dataset is complex, and in specific cases this complexity may
370 preclude thermal history interpretation (at this time) without a proper understanding of the
371 kinetics governing REA or at the very least, differences between fission track and α-damage

372 annealing rates. However, we discuss some possible ways forward when dealing with AFT and
373 accompanying elemental data from slowly-cooled terranes, which may serve as a framework to
374 assist in future interpretation.

375

376 A plot of central AFT age/MTL versus eU is shown in figure 2A, B. This visualization of AFT
377 data (generally utilizing ^{238}U only) has been the convention for previous studies addressing REA
378 (e.g. Hendriks and Redfield, 2005; Kohn et al., 2009). However, central age plots are non-ideal
379 for displaying age-eU relationships because of the modal tendency of this metric, which masks
380 high age scatter between individual grains. In our case there is large geographic distance between
381 sample locations and discrete thermal histories should be expected for each sample, yet there is a
382 consistent decrease in age with increasing eU. Our apatites are relatively mono-compositional.
383 Apatites characterized by >0.35 wt. % Cl (>0.1 apfu) are considered structurally controlled by Cl
384 and imply higher fission track retentivity (Barbarand et al., 2003), whereas our data are almost
385 entirely low retentivity F-apatite (fig. 2C) or from apatite varieties with greater hydroxyl and Ca-
386 site cation substituents (e.g. REE-rich F-apatite) There is also the possibility that a very minor
387 apatite component (<10 grains total) is in the belovite or britholite groups based on wt. % P_2O_5
388 (Pan and Fleet, 2002). Radial plots are useful for assessing mixtures of single-grain ages and
389 AFT age precision (Galbraith, 1990). All of our samples fail the χ^2 test when plotted on radial
390 plots, indicative of high age dispersion (fig. 3). Detrital AFT data often fail the χ^2 test due to
391 variable provenance (and composition), however for slowly-cooled bedrock samples failure may
392 be expected, d□□□□□ the range of single grain kinetic responses to annealing under slow-
393 cooling conditions (Galbraith and Laslett, 1993). An interesting feature of these data overall are
394 that samples with fewer grains typically have much lower dispersion (fig. 3), which is probably a
395 result of "under-sampling" and is an issue that may be unwittingly pervasive in older vintage
396 AFT datasets from slowly-cooled terrains.

397

398 Fission track length distributions for each sample are shown in figure 4, and in the absence of
399 thermal modeling, can be qualitatively assessed to understand thermal history complexity to first
400 order. Length distributions are presented as frequency (%) in 1 μm bins with equivalent normal
401 distributions shown for the mean ± 1σ (solid, blue curve) and the mode (dashed, red curve). The

track length distributions are mostly unimodal and shortened (centered at ~12-13 μm), signifying monotonic slow cooling or slow cooling and reheating (partial annealing) to ~65-80°C (Gleadow et al., 1986). Bimodal distributions, skewed distributions, or those with 'shoulders' can signify single-phase reheating to higher temperatures of ~80-100°C or episodic reheating in the partial annealing zone (~60-110°C; Gleadow et al., 1986). Baffin Island sample 09SRB-M100 and Melville Peninsula sample SNB-01-M2055 are examples that exhibit "out-of-phase" mean and mode distributions (fig. 4), which is indicative of bimodality and implies multi-stage thermal histories (ignoring differences in *n* tracks). These areas are both characterized by geologic and thermochronologic evidence of Paleozoic and/or Mesozoic burial (McDannell et al., 2019; Pinet et al., 2016).

We discuss the geologic context and other relevant high-temperature dating performed on each sample (when applicable) for each Canadian AFT sample below. All samples have summarized AFT information in the text and table 1. Likewise, all published samples are presented and discussed with known information relevant to their histories.

4.1 Western Superior Province

Sample PBA-98-743 is from a biotite tonalite-gneiss in the Harmon Lake Gneiss Complex of the Wabigoon Subprovince. The gneiss has a mean $^{207}Pb/^{206}Pb$ zircon core metamorphic protolith age of 2890 ± 8 Ma (MSWD=1.1) and a U-Pb titanite age of 2678 ± 2 Ma (Percival et al., 2004). The corresponding sample apatite U-Pb mixture model single age peak is 2971 ± 174 Ma (2σ; n=25). The AFT sample has a pooled age of 572.3 ± 15.6 Ma (1σ; n=40) and a central age of 597 ± 37 (1σ) with 36% age dispersion. The mean track length (MTL) is 12.07 ± 1.94 μm (1σ; n=130). The mean kinetic parameters for PBA-98-743 are: measured D_{par} of 1.89 μm, eU of 7 ppm (range 1-19 ppm), calculated r_{mr0} of 0.84, and measured Cl of 0.008 apfu.

Sample 03-GRS-013 is from a tonalite-quartz diorite in the Mesoarchean Sachigo Subprovince. The apatite U-Pb mixture model single age peak is 3009 ± 94 Ma (2σ; n=29). The AFT sample has a pooled age of 414.0 ± 14.1 Ma (1σ; n=40) and a central age of 447 ± 34 (1σ) with 46% age dispersion. The MTL is 12.51 ± 1.63 μm (1σ; n=131). The mean kinetic parameters for 03-GRS-

013 are: measured D_{par} of 1.91 μm, eU of 33 ppm (range 1-241 ppm), calculated r_{mr0} of 0.84, and measured Cl of 0.003 apfu.

4.2 Slave Province

Sample 12-DRA03-001 is from a plagioclase-bearing porphyritic intrusion with a turbidite deposit near Wheeler Lake in the Northwest Territories. This sample is at the approximate location of the Isachsen and Bowring (1994) lithic tuff sample (within turbidites) that has a reported U-Pb zircon age of 2612 ± 1 Ma. The sample apatite U-Pb mixture model single age peak is 2628 ± 96 Ma (2σ; n=36). The AFT sample has a pooled age of 335.7 ± 11.3 Ma (1σ; n=40) and a central age of 344 ± 14 (1σ) with 22% age dispersion. The MTL is 12.04 ± 2.39 μm (1σ; n=131). The mean kinetic parameters for 12-DRA03-001 are: measured D_{par} of 1.87 μm, eU of 16 ppm (range 2-55 ppm), calculated r_{mr0} of 0.83, and measured Cl of 0.019 apfu.

Sample BNB97-035 is plutonic med-coarse grained biotite granitoid with strong lineations taken from the west flank of the Sleepy Dragon Complex in the Yellowknife Domain of the Slave craton with nearby basement crystallization ages of ca. 2900 Ma (Bleeker et al., 1999), similar to the sample apatite U-Pb mixture model single age peak of 2858 ± 124 Ma (2σ; n=22). The AFT sample has a pooled age of 229.3 ± 22.1 Ma (1σ; n=40) and a central age of 272 ± 16 (1σ) with 34% age dispersion. The MTL is 12.75 ± 1.80 μm (1σ; n=116). The mean kinetic parameters for BNB97-035 are: measured Dpar of 1.72 μm, eU of 21 ppm (range 0.2-98), calculated r_{mr0} of 0.85, and measured Cl of 0.006 apfu.

Sample 12NK-L18A3 is from granitic gneiss in Nunavut with a zircon U-Pb age of 2487 ± 5.4 Ma and a metamorphic overprint U-Pb age of 2377 ± 3.5 Ma (Davis et al., 2014). The apatite U-Pb mixture model single age peak is significantly younger at 1788 ± 40 Ma (2σ; n=24). The AFT sample has a pooled age of 392.4 ± 9.0 Ma (1σ; n=26) and a central age of 397 ± 13 (1σ) with 14% age dispersion. The MTL is 11.91 ± 2.06 μm (1σ; n=78). The mean kinetic parameters for 12NK-L18A3 are: measured Dpar of 1.85 μm, very high eU of 339 ppm (range 139-655), calculated r_{mr0} of 0.79, and measured Cl of 0.012 apfu.

4.3 Churchill-Rae Province, Melville Peninsula region

Sample SNB-01-M2055 is from Melville Peninsula, ~150 km southwest of Committee Bay and is a foliated biotite tonalite that cuts a komatiite at the base of the Howling Wolf section with an U-

459 Pb zircon igneous crystallization age of 2606 ± 4 Ma (Cairns et al., 2005). The apatite U-Pb
460 mixture model single age peak is 1940 ± 68 Ma (2σ; n=26). The AFT sample has a pooled age of
461 348.5 ± 9.8 Ma (1σ; n=30) and a central age of 356 ± 18 (1σ) with 24% age dispersion. The
462 MTL is 12.19 ± 2.30 μm (1σ; n=130). The mean kinetic parameters for SNB-01-M2055 are:
463 measured D_{par} of 2.00 μm, eU of 14 ppm (range 0.2-46 ppm), calculated r_{mr0} of 0.84, and
464 measured Cl of 0.003 apfu.

465 *Sample 10CXAD-086A* is from eastern Melville Peninsula on the Foxe Basin margin and was
466 collected from a plutonic gabbro-anorthosite with nearby detrital U-Pb ages of 1899 ± 7 Ma and
467 1897 ± 15 Ma in the overlying Paleoproterozoic Penrhyn Group (Partin et al., 2014). The sample
468 apatite U-Pb mixture model single age peak is 1803 ± 73 Ma (2σ; n=24). The AFT sample has a
469 pooled age of 363.1 ± 28.5 Ma (1σ; n=40) and a central age of 460 ± 44 (1σ) with 57% age
470 dispersion. The MTL is 12.60 ± 1.79 μm (1σ; n=132). The mean kinetic parameters for
471 10CXAD-086A are: measured D_{par} of 2.12 μm, eU of 13 ppm (range 0.2-73 ppm), calculated r_{mr0}
472 of 0.82, and measured Cl of 0.029 apfu.

473 *Sample 11CXAN017* is from the Prince Albert block on Melville Peninsula and was collected
474 from a Neoarchean Bt-Kfs porphyritic monzogranite. The sample apatite U-Pb mixture model
475 single age peak is 1676 ± 59 Ma (2σ; n=18). The AFT sample has a pooled age of 418 ± 11 Ma
476 (1σ; n=18) and a central age of 452 ± 31 (1σ) with 28% age dispersion. The MTL is 12.67 ± 1.92
477 μm (1σ; n=120). The mean kinetic parameters for 11CXAN017 are: measured D_{par} of 1.95 μm,
478 eU of 21 ppm (range 3-43 ppm), calculated r_{mr0} of 0.85, and measured Cl of 0.002 apfu.

479 *Sample 13LVA04* is from a gabbro at the Discovery outcrop that cuts a banded iron formation
480 and the Sam Fm. at the Thelon Basin in S. Nunavut. The apatite U-Pb mixture model single age
481 peak is 2224 ± 125 Ma (2σ; n=39). The AFT sample has a pooled age of 546.0 ± 33.8 Ma (1σ;
482 n=40) and a central age of 557 ± 31 (1σ) with 21% age dispersion. The MTL is 12.44 ± 2.06 μm
483 (1σ; n=121). The mean kinetic parameters for 13LVA04 are: measured D_{par} of 1.92 μm, eU of 7
484 ppm (range 3-42 ppm), calculated r_{mr0} of 0.80, and measured Cl of 0.012 apfu.

485 *Sample 09SZ-23-01* is from Precambrian granitic gneiss at the northern margin of Melville
486 Peninsula at the Fury and Hecla Strait, <200 m from the Paleozoic unconformity presented in
487 Pinet et al. (2016). The AFT sample has a pooled age of 462.7 ± 29.9 Ma and a central age of
488 486 ± 27 Ma with 21% age dispersion. The MTL is 12.18 ± 1.58 μm (1σ; n=100). The mean

kinetic parameters for 09SZ-23-01 are: measured D_{par} of 1.67 μm, ^{238}U of 6 ppm (range 3-12 ppm), calculated r_{mr0} of 0.85, and measured Cl of 0.016 apfu. There are no apatite U-Pb data for this sample but there are coexisting apatite (U-Th)/He data with a weighted mean age of 347 ± 65 Ma (1σ; n=5) and an additional nearby (U-Th)/He sample 09SZ-24-01 with a weighted mean age of 211 ± 80 Ma (1σ; n=7). Sample 09SZ-23-01 is not entirely comparable to our ICP-MS AFT data because only ^{238}U was measured and is not necessarily representative of the eU, as Th and Sm contributions could make the eU much greater and add greater variability between grains. To add more approximate values for eU we took the average Th and Sm concentrations of the two apatite (U-Th)/He samples and used those to calculate eU for the AFT data. This yields a mean eU of 14 ppm (range 11-20 ppm). Further information regarding AFT analytical methods, Cl compositional data, and accompanying AHe data (sample 09SZ-24-01 at about the same location) are given in Lavoie et al. (2013) and Pinet et al. (2016).

4.4 Churchill-Rae Province, Southampton Island

Sample 07CYA-M38B is from gabbroic anorthosite bedrock on Southampton Island with a U-Pb zircon inherited primary crystallization age of 3005 ± 22 Ma and a recrystallization age of 1870 ± 10 Ma (MSWD=1.2) due to Trans-Hudson overprinting (Rayner et al., 2011). The apatite U-Pb mixture model single age peak is 1834 ± 60 Ma (2σ; n=35). The AFT sample has a pooled age of 341.6 ± 10.5 Ma (1σ; n=40) and a central age of 384 ± 21 (1σ) with 30% age dispersion. The MTL is 12.22 ± 2.0 μm (1σ; n=132). The mean kinetic parameters for 07CYA-M38B are: measured D_{par} of 1.90 μm, eU of 22 ppm (range 1-71 ppm), calculated r_{mr0} of 0.84, and measured Cl of 0.024 apfu.

Sample 07CYA-M133A is a plutonic diorite from Southampton Island with a U-Pb igneous crystallization age of 1842 ± 5 Ma (Rayner et al., 2011). The apatite U-Pb mixture model single age peak is 1812 ± 79 Ma (2σ; n=13). The AFT sample has a pooled age of 364.2 ± 10.6 Ma (1σ; n=15) and a central age of 375 ± 17 (1σ) with 16% age dispersion. The MTL is 11.57 ± 2.16 μm (1σ; n=101). The mean kinetic parameters for 07CYA-M133A are: measured D_{par} of 2.26 μm, eU of 74 ppm (range 7-258 ppm), calculated r_{mr0} of 0.80, and measured Cl of 0.086 apfu.

4.5 Rae craton, southern Baffin Island

517 *Sample 09SRB-M100* is a metasedimentary semipelite within the Paleoproterozoic Hoare Bay
518 Group at Kumlien Fiord on the Cumberland Peninsula, Baffin Island. The apatite U-Pb mixture
519 model single age peak is 1674 ± 35 Ma (2σ; n=28). The AFT sample has a pooled age of 97.2 ±
520 4.3 Ma (1σ; n=35) and a central age of 102 ± 8 (1σ) with 37% age dispersion. The MTL is 12.94
521 ± 2.23 μm (1σ; n=41). The mean kinetic parameters for 09SRB-M100 are: measured D_{par} of 2.14
522 μm, eU of 22 ppm (range 1-69 ppm), calculated r_{mr0} of 0.83, and measured Cl of 0.023 apfu.

523 *Sample 14SUB-H43A* is a metamorphic garnet-biotite psammite from a Paleoproterozoic
524 metasediment/layered mafic intrusion sequence on northern Hall Peninsula, Baffin Island. The
525 apatite U-Pb mixture model single age peak is 1782 ± 38 Ma (2σ; n=25). The AFT sample has a
526 pooled age of 440.2 ± 11.4 Ma (1σ; n=25) and a central age of 442 ± 12 (1σ) with 10% age
527 dispersion. The MTL is 12.46 ± 1.72 μm (1σ; n=130). The mean kinetic parameters for 14SUB-
528 H43A are: measured D_{par} of 2.29 μm, eU of 26 ppm (range 16-35 ppm), calculated r_{mr0} of 0.82,
529 and measured Cl of 0.022 apfu.

530 ***4.6 Grenville Orogen, southeast Quebec***

531 *Sample 02NKL-871* is from a granitic orthogneiss in southeast Quebec. It is shown here for
532 comparative purposes, as it is much younger (Grenvillian) than the majority of our other samples
533 taken from Archean bedrock. The apatite U-Pb mixture model single age peak is 951 ± 38 Ma
534 (2σ; n=25). The AFT sample has a pooled age of 160.8 ± 4.5 Ma (1σ; n=35) and a central age of
535 177 ± 13 (1σ) with 38% age dispersion. The MTL is 12.27 ± 1.80 μm (1σ; n=135). The mean
536 kinetic parameters for 02NKL-871 are: measured D_{par} of 1.83 μm, eU of 31 ppm (range 2-160
537 ppm), calculated r_{mr0} of 0.85, and measured Cl of 0.008 apfu. This sample will also be discussed
538 with AFT and AHe data from the Anticosti Island (Quebec) Grenville basement sample of
539 Powell et al., (2018a), see table 1.

540

541 **5. Discussion**

542 ***5.1 AFT age relationships between eU and kinetic parameters r_{mr0} and effective Cl***

543 Using plots of central age versus U, Hendriks and Redfield (2005) proposed that REA could
544 explain the observed decrease in AFT age with increasing U content for samples from the

Fennoscandian Shield. Kohn et al. (2009) compared central ages with eU values for a larger set of Precambrian shield rocks and reported weaker or inconsistent trends, suggesting that variable Cl content rather than REA was controlling AFT annealing and age dispersion. These contrasting results are not surprising given the methods that were used. Kinetic variability or potential REA effects should be evaluated for individual grains, particularly for the samples of this study that exhibit "open jaw" radial plots (O'Sullivan and Parrish, 1995; fig. 3) that are a common feature of multi-kinetic AFT samples (e.g. Issler et al., 2005; Powell et al., 2018b; Schneider and Issler, 2019). Furthermore, it can be difficult to infer compositional controls on AFT annealing using Cl content alone, when OH and various cations can also have a significant effect on AFT annealing (Barbarand et al., 2003; Carlson et al., 1999). Combining samples of different apatite composition and/or with different thermal histories may obscure any potential relationship between AFT age and eU.

Unlike the previous studies that used the external detector method where typically up to 20 age grains are measured, we use larger sets of AFT single grain ages (up to 40 grains per sample; table 1) obtained using the LA-ICP-MS method to investigate intra-sample age dispersion with respect to eU and annealing kinetic parameters derived from detailed elemental data. Samples with the largest number of measured grains (30-40) have the largest age dispersion (21-57%) whereas those with <30 grains have much lower dispersion (10-21%; fig. 3). Clearly it is necessary to measure a sufficient number of grains in order to sample as broad a range of eU values and AFT ages as possible. Although we also observe a weak negative correlation between central age and eU (fig. 2), single grain ages spanning hundreds of millions of years, or over a billion years in some cases, show a well-defined relationship between increasing eU and younger AFT age (fig. 5). Our bedrock AFT samples generally have near end-member fluorapatite compositions based on measured Cl concentration. Some samples show a broader range in track retentivity when other kinetic parameters such as r_{mr0} (or equivalent eCl) and D_{par}, are examined but there is no clear correlation between age and apatite composition (fig. 5). Instead, the extreme variations in eU seem to offer the best explanation for the observed AFT age heterogeneity (clear correlation with age, fig. 5). The effect of eU on fission-track retentivity may have a discernible link to long residence at low temperatures in or below the partial annealing zone.

575

576 The interplay between eU and the other dominant kinetic parameter (i.e. Cl) becomes complex in
577 some instances where Cl concentrations are comparatively variable or elevated, or there is
578 relative enrichment of cations such as Fe or REE (fig. 5 and fig. 6). This is clearly demonstrated
579 by a counterintuitive association between eU and eCl (or inverse correlation with r_{mr0}, fig. 6).
580 The Baffin Island semipelite sample 09SRB-M100C1 demonstrates a spurious correlation
581 between eU and eCl/r_{mr0}, which implies there is a confounding variable (e.g. thermal history) or
582 other kinetic parameter controlling retentivity. Higher eCl (and low r_{mr0}) values signify higher
583 retentivity, and high eU should hypothetically lower retentivity if greater damage is a proxy for
584 enhanced annealing. Chemically-retentive grains with elevated eU that have experienced a
585 thermal pulse may differentially anneal α-damaged FT regions with respect to grains that are
586 lower eCl, and suggest cumulative thermal annealing in this sample was sufficient to obscure
587 expected associations between retentivity proxies. A first-order filter for samples is examining
588 the AFT age-eU relationship. If a sample shows that eCl is heterogeneous in 'age-eU space' with
589 a clear negative (curvi-) linear age-eU correlation, then it can be assumed that eU is primarily
590 driving retentivity, see Southampton Island and Superior Province samples. If clear eCl
591 'domains' or divisions are apparent when viewing age-eU relationships (sample 09SRB-
592 M100C1), this suggests Cl or another cation-site element is playing a greater role in controlling
593 retentivity. Samples with more homogenous chemical compositions and low Cl show no such
594 relationship between eU and eCl/r_{mr0} and denote eU as a primary driver of intra-sample age
595 dispersion, which is reflected in plots of eU versus age that show age scatter across the entire
596 range of Cl. There is likely some threshold where Cl begins to counteract the effects of REA or
597 dominates fission-track retention, however this seems variable between samples and conceivably
598 has an association with thermal history.

599 ***5.2 Elemental substitutions and compositional variation***

600 The formula for apatite when considering substitutions (Barbarand et al., 2003) can be written as
601 $X_{10}YO_4Z_2$ where, X = mainly Ca, Y = P, and Z = F, Cl, or OH. The most common substitutions
602 on the X site are Fe^{2+}, Mn^{2+}, Na^{+}, REE^{3+} Sr^{2+} and U^{4+}, whereas Si and S occur on the Y site. The
603 trivalent (REE^{3+}) cations substitute in pairs to maintain charge balance: $REE^{3+} + Si^{4+}$ proceeds to
604 $Ca^{2+} + P^{5+}$ and $REE^{3+} + Na^{+}$ to $2Ca^{2+}$ (Barbarand et al., 2003 and refs. therein). Cation

substitutions directly govern the structural integrity of the apatite lattice and there is an inverse correlation between the number of substitutions on the cation (X) and anion (Z) sites (Carpéna, 1998). It has also been shown that preferential U and Th substitution in fluorapatite or chlorapatite causes a change in volume (decrease and increase, respectively) of the apatite Ca (I) and Ca (II) polyhedron (e.g. Carpéna et al., 1988; Carpéna, 1998; Luo et al., 2009). This change results in an increase in size and distortion of the Ca (II) site, allowing for preferential substitution of U and Th at both Ca sites in chlorapatite and is an interesting observation because the Carlson et al., (1999) dataset documents that Ca substitutions tend to reduce annealing rates in apatite but may also depend on a complex relationship with mixing at the halogen site (i.e. F/Cl/OH). The results of Luo et al., (2009) demonstrate that U and Th are structurally preferred in chlorapatite, so it is expected that previous work attributed differences in AFT ages to Cl rather than eU, as Cl is a dominant control on track retentivity.

We show two examples where we try to further investigate the compositional controls on AFT grain ages from samples with high and low age dispersion. Sample PBA-98-743 from the Superior Province and 12NK-L18A3 from the northeast Slave craton are characterized by 36% and 14% dispersion, respectively (fig. 3). PBA-98-743 exhibits strong eU control on age (figs. 4 and 6), however 12NK-L18A3 does not (fig. 4). Moreover, the Slave sample is characterized by old ages despite high eU (high α-damage; see fig. 9), suggesting another kinetic control on retentivity.

Linear correlation matrices were performed on the elemental data (apfu, including OH estimates) for our samples to assess the dominant interactions between the known controls on retentivity (fig. 7; all samples shown in SI). The data were standardized first to reduce any extreme variance between elements. Correlation coefficients associated with positive correlations are shown in black and variables that are anti-correlated are in white with the size of the circle corresponding to larger or smaller correlation coefficients (fig. 7A). For the Superior Province sample all linear correlations are shown in fig. 7A, however to assess the robustness of the relationship, only those that correspond to p-values of ≤ 0.05 or pass at 95% confidence level were retained (fig. 7B). F and Cl are anti-correlated as expected and in this case eU is most highly correlated with Ce ($r = 0.68$), La ($r = 0.56$), Cl ($r = 0.50$), Y ($r = 0.46$), Mn ($r = 0.45$) and is anti-correlated with F ($r = -$

635 0.41). La and Ce are the most-highly correlated elements (r = 0.90). However, caution is advised
636 in interpreting these relationships because in some cases many of the grains contain low or
637 negligible elements but only a few grains are enriched and produce a statistically robust
638 correlation (fig. 7C), as is the case with eU and La/Ce. However, an overall assessment of
639 elemental abundances and apatite lattice site "preference" are contained in these data.

640 Figure 7D is a case where no clear age-eU relationship is observed and this is revealed in the
641 correlation matrix (p-values of ≤0.05) as eU is not robustly correlated with any other element.
642 The Slave craton sample is incorporating REE, Mn, Fe, Na, and Cl. The most highly correlated
643 elements are La-Ce (r = 0.97), Na-Cl (r = 0.79), Na-Mg (r = 0.76), Mn-Fe (r = 0.76), Mn-Y (r =
644 0.74), Fe-Y (r = 0.66), and Fe-La (r = 0.63). A relationship that is clear from our samples is that
645 the preferential incorporation of cation elements such as REE and U-Th (table 2) seems to
646 dominate in cases where AFT ages exhibit a negative age-eU relationship, suggesting a dominant
647 retentive control on age due to elevated eU, which agree with the results of Carpéna (1998). Our
648 elemental data suggest that in addition to common apatite varieties, we may have more "exotic"
649 apatites that heavily incorporate REE, Na, U, and Si. We have not probed for Si but that may be
650 important to monitor in future AFT studies. These associations yield some insight into retentivity
651 (AFT age) and they indicate the elements that are being incorporated into apatite grains from a
652 particular bedrock sample, which may ultimately and indirectly aid in assessment of age
653 dispersion. Our correlation matrices (see SI) also demonstrate that fluorapatite is characterized
654 by lower Cl and U-Th affinity, whereas chlorapatite shows a positive correlation between Cl and
655 eU. These relationships also suggest that if actinides are incorporated into chlorapatite, then there
656 may be a delicate balance between elevated eU (retentivity decrease) and elements that are
657 known to increase track retentivity, which may be ultimately governed by damage accumulation
658 time and specific elemental abundance. It is extremely important to point out that while many of
659 these elements are highly correlated with one another, eU is the only element that exhibits a very
660 consistent and strong (curvi)-linear relationship with AFT single-grain ages in virtually all of our
661 samples. This observation advocates for α-radiation as a governing factor for AFT annealing in
662 slowly-cooled settings.

663

664 ***5.3 Enhanced dissolution and fission track etching rates***

Previous work has demonstrated α-radiation-enhanced dissolution is a concern for U-rich or actinide-bearing accessory mineral phases (e.g. Dran et al., 1984; Petit et al., 1985). Petit et al. showed that implantation of low energy (~1 keV/amu) Pb ions, which simulate α-recoil, greatly increases dissolution rate above a certain critical damage threshold of ~2.5×10^{18} α/g, dependent upon mineral U (Th and Sm) concentrations and accrued time of damage accumulation. Weber and Matzke (1986) examined actinide-host phases, one of which was the apatite structure $Ca_2Nd_8(SiO_4)_6O_2$ that was doped with ^{244}Cm to investigate the effects on microstructure from self-irradiation by α-decay and fission. They found that α-damage and fission tracks overlap at high doses and leads to amorphization at ~1.1×10^{19} α/g, ~8% swelling of the crystalline volume, and a factor of 10 increase in leachability. Ewing et al. (1981) document similar enhanced dissolution (by a factor of ~100) in increasingly older zircons with greater accumulated damage. Intuitively or hypothetically, if higher U caused enhanced track annealing, the FT analyst could measure the track lengths on grain mounts where U has also been directly obtained and observe a positive correlation between shorter lengths and higher U. We have examined some unpublished samples where we have U from both age and length grains and there is no clear relationship between length and U, accounting for both measured and c-axis projected lengths. This may be due to any number of factors affecting track length collection, such as differences in etching conditions (e.g. etch time, temperature, or acid strength), etching and/or annealing anisotropy, variability in measured length with respect to the c-axis, U heterogeneity, or simply and most importantly, the sub-random sampling of tracks for measurement. However, high U apatite (highly damaged) may reveal apparently longer tracks because short tracks are difficult to observe on a high track density surface – invalidating the assumption of high eU being correlated with shorter tracks and suggesting that the observation of longer tracks may be more likely for high eU grains. Ultimately, for AFT dating there may be no discernible differences in etching for typical apatites because the induced α-damage levels in laboratory experiments are rarely achieved in the geological environment.

5.4 Considering α-recoil and fission track damage accumulation and annealing

The α-damage present in apatite will increase with time as a function of the parent nuclide content, but will also decrease with heating (Shuster and Farley, 2009). The negative age-eU

695 trends in our dataset (not commonly observed for apatite data) imply long residence at low
696 temperatures below those required for track annealing (or significant He retention). Our data
697 empirically support the persistence of α-recoil damage over extremely long timescales in the
698 AFT system (figs. 8 and 9) and that α-damage is characterized by slower annealing rates than
699 fission-track damage, as previously suggested (e.g. Fox and Shuster, 2014; Ritter and Märk,
700 1986; Willett et al., 2017).

701

702 We further interrogate our AFT samples by estimating the amount of α-damage they have
703 accumulated. Alpha dose is calculated following equation 5 of Nasdala et al. (2005) and is
704 expressed as α/g.

705 $$D_\alpha = 8 \cdot \frac{C_U \cdot N_A \cdot 0.9928}{M_{238} \cdot 10^6} \cdot \left(e^{\lambda 238 t} - 1\right) + 7 \cdot \frac{C_U \cdot N_A \cdot 0.0072}{M_{235} \cdot 10^6} \cdot \left(e^{\lambda 235 t} - 1\right) + 6 \cdot \frac{C_{Th} \cdot N_A}{M_{232} \cdot 10^6} \cdot \left(e^{\lambda 232 t} - 1\right) \quad (1)$$

706 Where, C_U and C_{Th} are the actinide concentrations in ppm, N_A is Avogadro's number, and M_{238}
707 (etc.) are the molecular weights of the parent isotopes, and λ_{238}, λ_{235}, λ_{232} are the decay constants
708 for each. The *t* in the equation refers to the integration or accumulation time for α-particle self-
709 irradiation. Traditionally, for zircon this time is taken as the time since crystallization and is
710 presumably a reasonable assumption, however this becomes more difficult to assess for other
711 minerals such as apatite that are more prone to greater damage annealing at moderate
712 temperatures of <200°C.

713 The most difficult assumption regarding α-dose estimation is the integration time for self-
714 irradiation, and here we refer to the integration time as the "effective dose accumulation time"
715 (t_{EDA}). Typically it is believed that α-damage is fully annealed at temperatures of ~150°C (Weber
716 et al., 1997) and if fission tracks are fully annealed at ~125°C (Green et al., 1986) then the oldest
717 AFT age would yield a conservative estimate for t_{EDA}. A limitation in adhering to strict
718 temperature limits is that apatite composition can introduce differences in the thermal sensitivity
719 of an individual grain, and that the time spent at a given temperature is just as important, if not
720 more so for cratonic rocks. The trade-off between time and temperature, with respect to
721 annealing, is analogous to laboratory annealing experiments where the same degree of annealing
722 can be achieved at higher temperatures in a shorter time, or at lower temperatures over a longer
723 duration. Therefore, we optimistically estimate the t_{EDA} for apatite as the mean of the 2σ

724 minimum apatite U-Pb isotopic sum age for the sample. The apatite U-Pb age estimate for AFT
725 t_{EDA} seems to be a suitable approximation, however this should not be viewed as a rigorous
726 temperature-based appraisal because the large U-Pb apatite errors are in essence providing a
727 crude intermediary between the oldest representative AFT age (~track retention age) and isotopic
728 closure for the U-Pb system. We are currently more interested in observing data trends rather
729 than establishing absolute relationships, and as more data are collected on the ^{238}U percolation
730 dose threshold and the temperatures at which α-damage accumulation in different apatite
731 compositions is appreciable, there can be improvements to this approach as the t_{EDA} uncertainties
732 are high.

733

734 An example of the relationship between α-damage and cooling age is shown in figure 8 where
735 AFT and AHe data from the same location (Pinet et al., 2016) are plotted against eU and
736 transposed into α-dose. The apatite grains show a modest range in eU but interestingly the AFT
737 data only capture the low eU and the AHe data have a greater spread in eU (fig. 8A,B). This
738 observation certainly suggests preferential selection of grains for each method, perhaps outside
739 of the established routine of choosing pristine whole grains for (U-Th)/He analysis. The black
740 dashed line is the ^{238}U α-recoil track percolation threshold of $1.9x10^{16}$ α/g from Ketcham et al.,
741 (2017) and is the point where diffusivity is expected to increase due to damage connectivity
742 creating fast-path diffusion for the (U-Th)/He system. These data clearly demonstrate the
743 increase in AHe age going from low eU/low α-dose and increasing in age until the percolation
744 threshold is reached whereby a decrease in age follows (this is very similar to the observed
745 behaviour for zircon U-Th/He data for fission-track percolation Guenthner et al., 2013). The
746 AFT data are mostly above the U percolation threshold even though those grains have low eU,
747 whereas the AHe grains have higher eU concentrations/damage and are even younger. The
748 chronometer ages plot above the damage threshold due to long t_{EDA}, which dominates any effects
749 of high or variable eU between single grains. When examining samples, the difference in t_{EDA}
750 can explain why very different U and Th amounts between samples can result in similar overall
751 age-eU trends. Visually the data display remarkable adherence to the α-recoil track percolation
752 threshold, despite the fact that the data are from different thermochronometers, suggesting α-
753 damage affects apatite diffusive processes and has repercussions for both damage annealing and

diffusivity. Sample 13JP10 from the Grenville basement of Anticosti Island (Powell et al., 2018a) potentially spent ~275 Ma at temperatures >120-150°C, or experienced an episodic pulsed history to these high temperatures, which suggests that thermal resetting completely decoupled α-damage and fission track damage accumulation from one another (fig. 8C,D). It is also worth mentioning that 13JP10 underwent significant thermal annealing and is also one of the only samples shown in figure 2 with 40 dated age grains and low age dispersion (16%).

Our α-dose plots imply that at least some fission tracks are impacted by α-recoil tracks. At this time it is not entirely clear why AFT ages behave similarly to AHe ages with respect to the recoil damage percolation threshold, however it may be due to their shared dependence on diffusive mechanisms that affect track annealing and ^{4}He retentivity. We envision difficulty in trying to develop a model to jointly explain these damage types, as the dimensions, frequencies, and timescales (t_{EDA}) are very different. Now we examine our Canadian Shield AFT data with respect to the ^{238}U α-recoil percolation threshold and discuss these relationships.

Figure 9A shows AFT data from the Canadian Shield selected from table 1. All AFT samples with long (and similar) t_{EDA} >1 Ga plot to the right of the damage threshold, whereas Grenvillian basement samples 02NKL-871 and 13JP10 from Powell et al. (2018a) with shorter t_{EDA} <1 Ga show an increase and subsequent decrease in AFT ages before and after the damage threshold, respectively. To better understand the damage relation with AFT age, it is notable that a very high eU sample 12NK-L18A3 displays high damage and high eU variance (σ^2) between single grains (mean eU: 339 ± 158 ppm, 1σ) resulting in a relatively low spread in single-grain ages (403 ± 71 Ma (2σ, n=26)) but moderate spread in damage level. There is no clear age-eU relationship for this sample (fig. 5). Conversely, sample 13LVA04 has very low eU (and low σ^2; mean eU: 6 ± 1 ppm) and plots on the percolation threshold resulting in extreme age variability (560 ± 329 Ma (2σ, n=40)). High age scatter is expected for samples exhibiting high eU variability and especially for those near the percolation threshold – as this would be the region of greatest sensitivity to subtle changes in crystal damage and therefore changes in track annealing and effects on AFT age.

We also chose younger samples from the recent literature that have been dated by AFT and U-Pb (when possible) to compare to our Canada dataset. AFT samples from younger bedrock terranes in active tectonic settings including those from Sakhalin Island (Okhostsk), Russia (Glorie et al., 2017), the Yukon-Tanana area of central Alaska (Dusel-Bacon et al., 2016), the Wrangellia Terrane near Mt. Logan, Alaska (Enkelmann et al., 2017), and the northern Chilean Andes (Rodríguez et al., 2018). We also compared these to single-grain analyses of the Durango (eU = 81 ± 7 ppm, 1σ, n=300) and Fish Canyon Tuff (eU = 42 ± 15 ppm, n=300) AFT standards dated by P. O'Sullivan. This comparison was done to assess if there is similar behaviour with respect to damage accumulation and adherence to the α-recoil percolation threshold that is demonstrated by our older cratonic samples. The major limitation for finding suitable published data is that the majority of studies do not publish single-grain AFT analyses (only AFT sample summaries) and that apatites from younger rocks are not typically dated via LA-ICP-MS U-Pb because it is impractical due to the low amounts of U, Th, and Pb and the high initial common Pb incorporated in apatite (Chew et al., 2011). Published samples where Th was not reported or the EDM was used, we simply used the U amount to estimate the α-dose (Wrangellia and Russia), and examples where U-Pb data was unavailable we used the oldest individual AFT grain age or another high-T thermochronometer, i.e. $^{40}Ar/^{39}Ar$ biotite for Wrangellia to estimate t_{EDA}.

We give a brief description of each sample here, although for more complete information the reader should consult the cited reference. The Russian Sakhalin Island sample SK14-03 comes from a granodiorite with a zircon U-Pb age of 43.3 ± 0.6 Ma and an apatite U-Pb age of 38.9 ± 5.5 Ma. Twenty-six single-grain LA-ICP-MS AFT analyses yield a pooled age of 19.3 ± 2.1 Ma and central age of 18.4 ± 1.6 Ma (avg. ^{238}U=32 ppm; Glorie et al., 2017). The Yukon Alaska sample 09AD-240 is from a leucogranite with a SHRIMP zircon U-Pb igneous crystallization age of 191 ± 5 Ma and a pooled fission track age of 48.9 ± 3.9 Ma (avg. eU=12 ppm, n=40). The t_{EDA} for this sample was estimated by evidence that Mesozoic granitoids intruded the country rock and cooled to <300°C by ~185 Ma (Dusel-Bacon et al., 2016). Sample LL07 was collected from the Chilean Andes Main Cordillera north of 31.5°S from the Upper Cretaceous-Paleocene intrusive belt (Rodríguez et al., 2018). This sample has an AFT age of 31 ± 1.8 Ma (avg. eU=73

ppm, n=40) with a biotite K/Ar age of c. 67 Ma, taken as an approximation for t_{EDA} (all ages are quoted at the 1σ level).

Figure 9B shows that all of the younger samples from the literature plot to the left of the α-recoil percolation threshold and do not display the same age-dose patterns as the old cratonic samples. This further demonstrates that apatites characterized by high or variable eU still require significant time to accumulate radiation damage to produce an effect on AFT ages.

5.5 Multi-kinetic interpretation and thermal history modeling

The goal of most AFT studies is to model the age and track length data to make inferences about past thermal history and geologic processes. This can only be achieved if we have a robust understanding of the kinetics that govern the thermochronometers that we use. There are multiple fission track annealing proxies such as measured Cl, r_{mr0}, and D_{par} that assist us in deconvolving the annealing complexity contained within samples, however these tools are not perfect and in some cases offer little help in understanding multi-kinetic samples. Our Canadian Shield samples are typically compositionally homogeneous, which makes multi-kinetic interpretation exceedingly problematic. Figure 10 shows two examples of an exploratory attempt at utilizing the AFT age-α-dose (eU) relationship that is common to all of our cratonic samples. Samples 02NKL-871 and 11CXAN017 are very different in terms of calculated t_{EDA} and are used as examples for multi-kinetic interpretation. We display the grain ages for each sample on a radial plot (fig. 10 A, E) and perform age mixture modeling as before to identify statistically significant age populations. These age populations are then plotted in terms of their eCl (fig. 10B, F) and there is complete overlap between all populations, which invalidates clear compositional separation due to chemical homogeneity between grains spanning the typical eCl error range. If traditional compositional proxies suggest our sample is probably common F-apatite (fig. 10B, F), but there is high age dispersion, we can be certain that another factor such as eU may be controlling retentivity (fig. 10C, G). When these samples are examined in terms of α-dose it becomes obvious that there are grains of similar age – for different reasons. The low eU grains for sample 02NKL-871 have accumulated less damage or are generally low retentivity that have probably experienced some thermal annealing, whereas the high eU/highly damaged grains have experienced REA. There is undoubtedly a competition between fission track and α-damage ingrowth and annealing that occurs and is further complicated by minor thermal annealing

842 events, as fission tracks and α-damage vary in both temperature sensitivity and natural
843 abundance. The same level of thermal annealing would preferentially remove more fission
844 damage, but the remaining α-damage would still play a role in overall retentive behaviour. The
845 separation of kinetic populations is more apparent for grains that have migrated across the α-
846 recoil percolation threshold due to longer t_{EDA} (fig. 10H). The age peaks picked by the radial plot
847 mixture modeling are based on age (and U-related age precision) and match the age populations
848 identified by the differences in α-dose between the two groups for sample 11CXAN017. In these
849 cases we have identified a potential path forward in terms of separating kinetic populations by
850 eU or α-dose for apatites in slowly-cooled rocks.

851 ***5.6 Implications for the apatite fission track and (U-Th)/He thermochronometers***

852 Carpéna et al. (1988) discuss one of the earliest known examples of the effects of U-Th on AFT
853 ages from the In Ouzzal carbonatites in Africa where they suggested that higher radiation
854 damage causes apatite lattice expansion and increases the thermal sensitivity of fission tracks to
855 thermal annealing events. Carpéna and Lacout (2010) carried out thermal annealing experiments
856 on synthetic apatites doped with ^{235}U and irradiated with thermal neutrons to induce fission.
857 They compared the synthetic apatite (no α-damage) to natural apatite to demonstrate that fission
858 tracks in the synthetic apatite needed higher temperatures and longer time to reach the same
859 degree of annealing when compared to natural apatite. Experimental evidence has also shown
860 that α-particle irradiation-induced annealing occurs in buried amorphous layers in natural
861 Durango fluorapatite (Ouchani et al., 1997) and similar behaviour has been observed in silicate
862 apatite structures, which are more thermally stable than natural apatite (Weber et al., 1986;
863 Weber et al., 1997). The latter studies were performed on thick amorphous layers, which should
864 be more difficult to anneal than amorphous tracks, supporting the idea that fission track
865 annealing could be enhanced by α-radiation. Non-thermal annealing of α-recoil damage and
866 recovery of crystalline structure from (pre-damaged) fully-amorphous Durango apatite
867 specimens was observed by *in situ* transmission electron microscopy (Li et al., 2017). Damage
868 recovery through α-healing has also been recently demonstrated for monazite, suggesting that
869 natural monazite, like apatite, never becomes amorphous due to the effects of α-recoil (Seydoux-
870 Guillaume et al., 2018). These experiments and observations support REA and imply that cratons
871 would be the ideal natural laboratory because rocks reside at low temperatures (<100°C) over

872 hundreds of millions to billions of years favouring high α-damage accumulation in natural apatite
873 compositions. In the case of lower eU concentrations, a long t_{EDA} could also create the same
874 conditions for lowering annealing activation energy.

875

876 We are unsure if α-particles directly anneal fission tracks, as posited by Hendriks and Redfield
877 (2005), or that perhaps α-recoil acts to destabilize fission tracks and therefore affects annealing
878 rates. More work is required to properly evaluate the thermal and temporal sensitivity of
879 different apatite compositions and the kinetics of α-recoil and fission-track damage. The process
880 or mechanism by which α-recoil damage destabilizes fission tracks is not fully understood.
881 However, some hypotheses are that (1) lattice distortion from accrued α-damage may increase
882 the thermal annealing susceptibility of apatite, (2) α-decay ionization and electrical excitation
883 cause fission track defect annealing via self-heating over 100s-1000 My timescales, or (3) α-
884 damage interferes with or "connects" with fission-tracks directly, disrupting the crystal lattice,
885 which in turn yields a fission track configuration that is easier to anneal. Elemental substitutions
886 may act in a similar manner as hypothesis (3) by elements of different size or lattice site
887 affecting annealing behaviour.

888

889 We know that α-damage zones (Farley, 2000; Shuster et al., 2006), vacancies (Gerin et al.,
890 2017), porous voids (Zeitler et al. 2017), and dislocations (McDannell et al., 2018b) increase ^{4}He
891 retentivity and act as diffusive traps for (U-Th)/He dating. In the case of AFT analysis, REA may
892 be a purely structural effect from lattice distortions or convolved with the fact that in some cases
893 those substitutions happen to be high α-emitters, thus introducing the likelihood for the
894 degradation of fission-track integrity that is most evident when thermal annealing is a secondary
895 concern. We can envision the structural relaxation phase of α-damage annealing being very
896 important in apatite that has accumulated greater damage, which may lead to differences in
897 annealing due to enhanced lattice recovery during any thermal perturbation with respect to an
898 undamaged apatite. It is not clear how other Ca-site substituting elements such as Fe that
899 increase fission track retentivity, would play a role in counteracting REA and would obviously
900 only do so if present in sufficient quantity within the lattice. A corollary exists in zircon where
901 greater U and Th content increases microstructural deformation as further development and creep

of lattice dislocations cause enhanced diffusivity of these elements (Timms et al., 2006). Crystal lattice defects related to α-recoil might be a primary contributor to fission track instability. This could either be directly, or by association with substituting α-emitting parent nuclides such as U and Th. Interference between lattice defects due to α-recoil and fission-track defects could invariably result in α-recoil causing sufficient damage to facilitate annealing, especially given the rarity of fission tracks with respect to α-recoil tracks. These effects could presumably overwhelm apatite fission tracks from rocks with variable U and Th concentrations that have been residing at near-surface conditions for hundreds of millions of years. In other cases involving more complex shallow burial and exhumation events, some amount of α-damage may be preserved for up to a billion years or more and never fully annealed. In these scenarios, thermal annealing is mostly insignificant at <60°C, but α-induced damage could cumulatively modify the apatite lattice in proportion to the U and Th, making fission tracks unstable and driving differential annealing at low temperatures – thereby yielding large AFT single-grain age dispersion. This is likely amplified by longer damage accumulation times and is more noticeable in samples with a range of eU. Fission tracks and α-damage both undergo annealing via diffusive processes (Ritter and Märk, 1986), which are regulated by crystallographic damage level; therefore they should be viewed and treated as a damage continuum with different timescale and kinetic dependencies.

6. Recommendations and questions for future work

The effects of REA on AFT ages in slowly-cooled settings is a complex problem that requires sufficient data to be able to evaluate relationships between chemical composition and age. Some factors to consider in future work to assist in addressing REA include:

1. Acquire enough age grains to capture and to characterise intra-sample AFT age dispersion. We recommend counting a minimum of 35-40 grains (dependent on sample quality), especially given the ~10-20% dispersion for <25 measured grains versus ~30-40% dispersion for >30 grains quoted in figure 3.
2. Collect detailed elemental data for every sample including length and age grains; e.g. measured Cl is insufficient and could give misleading results. The acquisition of F, Na, Mg, P, S, Cl, Ca, Mn, Fe, Sr, Y, La, Ce, and Si at the very least should be carried out, since many of these elements are known to affect apatite damage retentivity. The

measurement of U, Th, and Sm on length grains (we did not do this for our samples) may also be beneficial for interrogating potential AFT length-eU relationships.

3. Acquire apatite U-Pb age data to estimate t_{EDA}. In cases where U-Pb data are lacking and a broad range of U has been sampled within an AFT dataset, the oldest reliably measured AFT age seems to be a satisfactory minimum time estimate of dose accumulation.
4. If cratonic bedrock samples are to be treated as multi-kinetic for thermal history modeling, evaluating grains in terms of eU may be a suitable kinetic proxy alternative for separating kinetic populations. The influence of apatite composition on annealing needs refinement and currently the choice of r_{mr0} equation is important and further work is needed to constrain the relationship at high and low retentivity where existing models do not sufficiently capture variability in retentivity.

7. Conclusions

Apatites from bedrock samples across many areas of the Canadian Shield show coincident high single-grain age dispersion and variable eU. There are no other clear intra-sample, compositional controls such as Cl, Fe, or REE substitution that demonstrate a strong relation with AFT age. In some isolated cases there are some grains enriched in elements known to enhance fission-track retentivity, however these are typically only a few grains from within a sample. The complexity of our AFT dataset further establishes the necessity of acquiring compositional data for interpreting apatite fission-track analyses and our data strongly support the notion that REA from α-damage is related to the eU content within apatite. We stress that this does not invalidate AFT analysis, although care should be taken to properly evaluate slowly-cooled rocks. Complications arise between co-existing, specific elemental substitutions that independently act to either enhance or reduce fission track annealing. The exact mechanism for enhanced annealing is likely multifaceted but may be due to α-damage affecting tracks directly, α-damage and elemental substitutions causing lattice defects that promote track instability and lower thermal annealing resistance, α-damage self-healing reducing lattice damage and affecting fission tracks, or a combination of these effects that are exacerbated in settings where thermal annealing is minimal and timescales for α-damage accumulation are long.

Acknowledgements

We thank W. Weber, R. Ewing, and R. Ketcham for discussions on radiation damage, and D. Shuster (editor) and J. Powell, C. Willett, and an anonymous reviewer for comments to strengthen the paper. This work was funded by the Geomapping for Energy and Minerals Program (GEM-II) through Natural Resources Canada, Land and Minerals Sector, Geological Survey of Canada and contributes to the Trans-GEM synthesis of the Canadian Shield Phanerozoic history. NRCan contribution number 20180216. Correlation matrix analyses performed using RStudio v. 1.1.453 (R Core Team, 2018) using the corrplot and cor.mtest packages (Wei and Simko, 2017). Other figures created using Generic Mapping Tools (GMT) v. 5.4 (Wessel et al., 2013).

References

Afra, B., Lang, M., Rodriguez, M.D., Zhang, J., Giulian, R., Kirby, N., Ewing, R.C., Trautmann, C., Toulemonde, M. and Kluth, P. (2011) Annealing kinetics of latent particle tracks in Durango apatite. Physical Review B 83, 064116.

Ault, A.K., Flowers, R.M. and Bowring, S.A. (2009) Phanerozoic burial and unroofing history of the western Slave craton and Wopmay orogen from apatite (U–Th)/He thermochronometry. Earth and Planetary Science Letters 284, 1-11.

Ault, A.K., Flowers, R.M. and Bowring, S.A. (2013) Phanerozoic surface history of the Slave craton. Tectonics 32, 1066-1083.

Bae, I.-T., Zhang, Y., Weber, W.J., Ishimaru, M., Hirotsu, Y. and Higuchi, M. (2007) Ionization-induced effects in amorphous apatite at elevated temperatures. Journal of Materials Research 23, 962-967.

Barbarand, J., Carter, A., Wood, I. and Hurford, T. (2003) Compositional and structural control of fission-track annealing in apatite. Chemical Geology 198, 107-137.

Baughman, J.S., Flowers, R.M., Metcalf, J.R. and Dhansay, T. (2017) Influence of radiation damage on titanite He diffusion kinetics. Geochimica et Cosmochimica Acta 205, 50-64.

Berman, R., Sanborn-Barrie, M., Rayner, N. and Whalen, J. (2013) The tectonometamorphic evolution of Southampton Island, Nunavut: Insight from petrologic modeling and in situ SHRIMP geochronology of multiple episodes of monazite growth. Precambrian Research 232, 140-166.

Berman, R.G., Davis, W.J., Corrigan, D. and Nadeau, L. (2015) Insights into the tectonothermal history of Melville Peninsula, Nunavut, provided by in situ SHRIMP geochronology and thermobarometry. Geological Survey of Canada, Current Research, p. 22.

Bleeker, W., Ketchum, J.W. and Davis, W. (1999) The Central Slave Basement Complex, Part II: age and tectonic significance of high-strain zones along the basement-cover contact. Canadian Journal of Earth Sciences 36, 1111-1130.

Burgess, P.M. (2008) Phanerozoic evolution of the sedimentary cover of the North American craton. Sedimentary basins of the world 5, 31-63.

Cairns, S., Relf, C., MacLachlan, K. and Davis, W. (2005) Neoarchean decoupling of upper-and mid-crustal tectonothermal domains in the southeast Slave Province: evidence from the Walmsley Lake area. Canadian Journal of Earth Sciences 42, 869-894.

Carlson, W.D. (1990) Mechanisms and kinetics of apatite fission-track annealing. American Mineralogist;(United States) 75.

Carlson, W.D., Donelick, R.A. and Ketcham, R.A. (1999) Variability of apatite fission-track annealing kinetics: I. Experimental results. American mineralogist 84, 1213-1223.

Carpéna, J. (1998) Uranium-235 fission track annealing in minerals of the apatite group: An experimental study, Advances in Fission-Track Geochronology. Springer, Dordrecht, pp. 81-92.

Carpéna, J. and Lacout, J.-L. (2010) Thermal annealing of fission tracks in synthetic apatites. Nuclear Instruments and Methods in Physics Research Section B: Beam Interactions with Materials and Atoms 268, 3191-3194.

Carter, A. (1990) The thermal history and annealing effects in zircons from the Ordovician of North Wales. International Journal of Radiation Applications and Instrumentation. Part D. Nuclear Tracks and Radiation Measurements 17, 309-313.

Chakoumakos, B.C., Murakami, T., Lumpkin, G.R. and Ewing, R.C. (1987) Alpha-decay-induced fracturing in zircon: The transition from the crystalline to the metamict state. Science 236, 1556-1559.

Chew, D.M. and Donelick, R.A. (2012) Combined apatite fission track and U-Pb dating by LA-ICP-MS and its application in apatite provenance analysis. Quantitative mineralogy and microanalysis of sediments and sedimentary rocks: Mineralogical Association of Canada Short Course 42, 219-247.

Chew, D.M., Sylvester, P.J. and Tubrett, M.N. (2011) U-Pb and Th-Pb dating of apatite by LA-ICPMS. Chemical Geology 280, 200-216.

Cookenboo, H.O., Orchard, M.J. and Daoud, D.K. (1998) Remnants of Paleozoic cover on the Archean Canadian Shield: limestone xenoliths from kimberlite in the central Slave craton. Geology 26, 391-394.

Corrigan, D., Nadeau, L., Brouillette, P., Wodicka, N., Houle, M.G., Tremblay, T., Machado, G. and Keating, P. (2013) Overview of the GEM Multiple Metals - Melville Peninsula project, central Melville Peninsula, Nunavut. Geological Survey of Canada, p. 17.

Crowley, K.D., Cameron, M. and Shaefer, R.I. (1991) Experimental studies of annealing of etched fission tracks in fluorapatite. Geochimica et Cosmochimica Acta 55, 1449-1465.

Davis, W.J., Berman, R.G., Nadeau, L. and Percival, J.A. (2014) U-Pb Zircon Geochronology of a transect across the Thelon Tectonic Zone, Queen Maud region, and adjacent Rae craton, Kitikmeot region, Nunavut, Canada, Open File 7652. Geological Survey of Canada, pp. 1-39.

Djimbi, D.M., Gautheron, C., Roques, J., Tassan-Got, L., Gerin, C. and Simoni, E. (2015) Impact of apatite chemical composition on (U-Th)/He thermochronometry: An atomistic point of view. Geochimica et Cosmochimica Acta 167, 162-176.

Donelick, R.A., Ketcham, R.A. and Carlson, W.D. (1999) Variability of apatite fission-track annealing kinetics: II. Crystallographic orientation effects. American mineralogist 84, 1224-1234.

Donelick, R.A., O'Sullivan, P.B. and Ketcham, R.A. (2005) Apatite fission-track analysis. Reviews in Mineralogy and Geochemistry 58, 49-94.

1044 Donelick, R.A., Roden, M.K., Mooers, J.D., Carpenter, B.S. and Miller, D.S. (1990) Etchable
1045 length reduction of induced fission tracks in apatite at room temperature (~23C):
1046 Crystallographic orientation effects and "initial" mean lengths. International Journal of
1047 Radiation Applications and Instrumentation. Part D. Nuclear Tracks and Radiation
1048 Measurements 17, 261-265.
1049 Duddy, I., Green, P. and Laslett, G. (1988) Thermal annealing of fission tracks in apatite 3.
1050 Variable temperature behaviour. Chemical Geology: Isotope Geoscience section 73, 25-
1051 38.
1052 Dusel-Bacon, C., Bacon, C.R., O'Sullivan, P.B. and Day, W.C. (2016) Apatite fission-track
1053 evidence for regional exhumation in the subtropical Eocene, block faulting, and localized
1054 fluid flow in east-central Alaska. Canadian Journal of Earth Sciences 53, 260-280.
1055 Enkelmann, E., Piestrzeniewicz, A., Falkowski, S., Stübner, K. and Ehlers, T.A. (2017)
1056 Thermochronology in southeast Alaska and southwest Yukon: Implications for North
1057 American Plate response to terrane accretion. Earth and Planetary Science Letters 457,
1058 348-358.
1059 Ewing, R.C., Haaker, R.F. and Lutze, W. (1981) Leachability of zircon as a function of alpha
1060 dose. MRS Online Proceedings Library Archive https://doi.org/10.1557/PROC-11-389.
1061 Ewing, R.C., Meldrum, A., Wang, L. and Wang, S. (2000) Radiation-induced amorphization.
1062 Reviews in Mineralogy and Geochemistry 39, 319-361.
1063 Ewing, R.C. and Weber, W.J. (2010) Actinide waste forms and radiation effects, The Chemistry
1064 of the Actinide and Transactinide Elements. Springer, Dordrecht, pp. 3813-3887.
1065 Farley, K.A. (2000) Helium diffusion from apatite; general behavior as illustrated by Durango
1066 fluorapatite. Journal of Geophysical Research 105, 2903-2914.
1067 Farley, K.A., Wolf, R.A. and Silver, L.T. (1996) The effects of long alpha-stopping distances on
1068 (U-Th)/He ages. Geochimica et Cosmochimica Acta 60, 4223-4229.
1069 Feinstein, S., Kohn, B., Osadetz, K., Everitt, R. and O'Sullivan, P. (2009) Variable Phanerozoic
1070 thermal history in the Southern Canadian Shield: Evidence from an apatite fission track
1071 profile at the Underground Research Laboratory (URL), Manitoba. Tectonophysics 475,
1072 190-199.
1073 Fitzgerald, P.G., Baldwin, S.L., Webb, L.E. and O'Sullivan, P.B. (2006) Interpretation of (U–
1074 Th)/He single grain ages from slowly cooled crustal terranes: A case study from the
1075 Transantarctic Mountains of southern Victoria Land. Chemical Geology 225, 91-120.
1076 Fleischer, R.L., Price, P.B. and Walker, R.M. (1965) Tracks of charged particles in solids.
1077 Science 149, 383-393.
1078 Flowers, R.M. (2009) Exploiting radiation damage control on apatite (U–Th)/He dates in
1079 cratonic regions. Earth and Planetary Science Letters 277, 148-155.
1080 Flowers, R.M. and Kelley, S.A. (2011) Interpreting data dispersion and "inverted" dates in
1081 apatite (U–Th)/He and fission-track datasets: An example from the US midcontinent.
1082 Geochimica et Cosmochimica Acta 75, 5169-5186.
1083 Flowers, R.M., Ketcham, R.A., Shuster, D.L. and Farley, K.A. (2009) Apatite (U–Th)/He
1084 thermochronometry using a radiation damage accumulation and annealing model.
1085 Geochimica et Cosmochimica Acta 73, 2347-2365.
1086 Fox, M. and Shuster, D.L. (2014) The influence of burial heating on the (U–Th)/He system in
1087 apatite: Grand Canyon case study. Earth and Planetary Science Letters 397, 174-183.

1088 Galbraith, R.F. (1990) The radial plot: graphical assessment of spread in ages. International
1089 Journal of Radiation Applications and Instrumentation. Part D. Nuclear Tracks and
1090 Radiation Measurements 17, 207-214.
1091 Galbraith, R.F. and Laslett, G.M. (1993) Statistical models for mixed fission track ages. Nuclear
1092 Tracks and Radiation Measurements 21, 459-470.
1093 Garver, J.I., Soloviev, A.V. and Reiners, P.W. (2004) Field observations of the stability of
1094 fission tracks in radiation-damaged zircon, 10th International Conference on Fission-
1095 Track Dating and Thermochronology, Amsterdam, p. 56.
1096 Gastil, R.G., DeLisle, M. and Morgan, J. (1967) Some effects of progressive metamorphism on
1097 zircons. Geological Society of America Bulletin 78, 879–906.
1098 Gautheron, C., Tassan-Got, L., Barbarand, J. and Pagel, M. (2009) Effect of alpha-damage
1099 annealing on apatite (U–Th)/He thermochronology. Chemical Geology 266, 157-170.
1100 Gautheron, C., Barbarand, J., Ketcham, R.A., Tassan-Got, L., van der Beek, P., Pagel, M., Pinna-
1101 Jamme, R., Couffignal, F. and Fialin, M. (2013) Chemical influence on α-recoil damage
1102 annealing in apatite: Implications for (U–Th)/He dating. Chemical Geology 351, 257-
1103 267.
1104 Gautheron, C., Tassan-Got, L., Barbarand, J. and Pagel, M. (2009) Effect of alpha-damage
1105 annealing on apatite (U–Th)/He thermochronology. Chemical Geology 266, 157-170.
1106 Gerin, C., Gautheron, C., Oliviero, E., Bachelet, C., Djimbi, D.M., Seydoux-Guillaume, A.-M.,
1107 Tassan-Got, L., Sarda, P., Roques, J. and Garrido, F. (2017) Influence of vacancy damage
1108 on He diffusion in apatite, investigated at atomic to mineralogical scales. Geochimica et
1109 Cosmochimica Acta 197, 87-103.
1110 Gibbons, J.F. (1972) Ion implantation in semiconductors—Part II: Damage production and
1111 annealing. Proceedings of the IEEE 60, 1062-1096.
1112 Gleadow, A. and Duddy, I. (1981) A natural long-term track annealing experiment for apatite.
1113 Nuclear tracks 5, 169-174.
1114 Gleadow, A.J., Duddy, I.R., Green, P.F. and Hegarty, K.A. (1986) Fission track lengths in the
1115 apatite annealing zone and the interpretation of mixed ages. Earth and Planetary Science
1116 Letters 78, 245-254.
1117 Glorie, S., Alexandrov, I., Nixon, A., Jepson, G., Gillespie, J. and Jahn, B.-M. (2017) Thermal
1118 and exhumation history of Sakhalin Island (Russia) constrained by apatite U-Pb and
1119 fission track thermochronology. Journal of Asian Earth Sciences 143, 326-342.
1120 Green, P. (1988) The relationship between track shortening and fission track age reduction in
1121 apatite: combined influences of inherent instability, annealing anisotropy, length bias and
1122 system calibration. Earth and Planetary Science Letters 89, 335-352.
1123 Green, P. and Duddy, I. (2006) Interpretation of apatite (U–Th)/He ages and fission track ages
1124 from cratons. Earth and Planetary Science Letters 244, 541-547.
1125 Green, P., Duddy, I., Gleadow, A., Tingate, P. and Laslett, G. (1986) Thermal annealing of
1126 fission tracks in apatite: 1. A qualitative description. Chemical Geology: Isotope
1127 Geoscience section 59, 237-253.
1128 Green, P., Duddy, I., Laslett, G., Hegarty, K., Gleadow, A.W. and Lovering, J. (1989) Thermal
1129 annealing of fission tracks in apatite 4. Quantitative modelling techniques and extension
1130 to geological timescales. Chemical Geology: Isotope Geoscience section 79, 155-182.
1131 Green, P.F., Crowhurst, P.V., Duddy, I.R., Japsen, P. and Holford, S.P. (2006) Conflicting (U–
1132 Th)/He and fission track ages in apatite: enhanced He retention, not anomalous annealing
1133 behaviour. Earth and Planetary Science Letters 250, 407-427.

1134 Guenthner, W.R., Reiners, P.W., Drake, H. and Tillberg, M. (2017) Zircon, titanite, and apatite
1135 (U-Th)/He ages and age-eU correlations from the Fennoscandian Shield, southern
1136 Sweden. Tectonics.
1137 Guenthner, W.R., Reiners, P.W., Ketcham, R.A., Nasdala, L. and Giester, G. (2013) Helium
1138 diffusion in natural zircon: Radiation damage, anisotropy, and the interpretation of zircon
1139 (U-Th)/He thermochronology. American Journal of Science 313, 145-198.
1140 Hasebe, N., Barbarand, J., Jarvis, K., Carter, A. and Hurford, A.J. (2004) Apatite fission-track
1141 chronometry using laser ablation ICP-MS. Chemical Geology 207, 135-145.
1142 Hendriks, B. and Redfield, T. (2005) Apatite fission track and (U-Th)/He data from
1143 Fennoscandia: An example of underestimation of fission track annealing in apatite. Earth
1144 and Planetary Science Letters 236, 443-458.
1145 Hendriks, B. and Redfield, T. (2006) Reply to: Comment on "Apatite Fission Track and (U–
1146 Th)/He data from Fennoscandia: An example of underestimation of fission track
1147 annealing in apatite" by BWH Hendriks and TF Redfield. Earth and Planetary Science
1148 Letters 248, 569-577.
1149 Hoffman, P.F., Bally, A. and Palmer, A. (1989) Precambrian geology and tectonic history of
1150 North America. The geology of North America—an overview, 447-512.
1151 Holland, H.D. and Gottfried, D. (1955) The effect of nuclear radiation of the structure of zircon.
1152 Acta Crystallographica 8, 291-300.
1153 Isachsen, C.E. and Bowring, S.A. (1994) Evolution of the Slave Craton. Geology 22, 917-920.
1154 Issler, D.R. and Grist, A.M. (2008) Reanalysis and reinterpretation of apatite fission track data
1155 from the central MacKenzie Valley, NWT, Northern Canada: Implications for kinetic
1156 parameter determination and thermal modelling, in: Garver, J.I., Montario, M.J. (Eds.),
1157 11th Internation Conference on Thermochronology. Abstracts with programs, Anchorage,
1158 Alaska, pp. 130-132.
1159 Issler, D., Grist, A. and Stasiuk, L. (2005) Post-Early Devonian thermal constraints on
1160 hydrocarbon source rock maturation in the Keele Tectonic Zone, Tulita area, NWT,
1161 Canada, from multi-kinetic apatite fission track thermochronology, vitrinite reflectance
1162 and shale compaction. Bulletin of Canadian Petroleum Geology 53, 405-431.
1163 Issler, D.R., Lane, L.S. and O'Sullivan, P.B. (2018) Characterisation, interpretation and
1164 modelling of multi-kinetic apatite fission track data using elemental data. Geological
1165 Survey of Canada, Scientific Presentation 94, 1 sheet, https://doi.org/10.4095/311302.
1166 Jackson, K. (1988) A defect model for ion-induced crystallization and amorphization. Journal of
1167 Materials Research 3, 1218-1226.
1168 Kasuya, M. and Naeser, C.W. (1988) The effect of α-damage on fission-track annealing in
1169 zircon. International Journal of Radiation Applications and Instrumentation. Part D.
1170 Nuclear Tracks and Radiation Measurements 14, 477-480.
1171 Ketcham, R.A. (2015) Calculation of stoichiometry from EMP data for apatite and other phases
1172 with mixing on monovalent anion sites. American mineralogist 100, 1620-1623.
1173 Ketcham, R.A., Carter, A., Donelick, R.A., Barbarand, J. and Hurford, A.J. (2007) Improved
1174 measurement of fission-track annealing in apatite using c-axis projection. American
1175 mineralogist 92, 789-798.
1176 Ketcham, R.A., Donelick, R.A. and Carlson, W.D. (1999) Variability of apatite fission-track
1177 annealing kinetics; III, Extrapolation to geological time scales. American mineralogist
1178 84, 1235-1255.

Ketcham, R.A., Gautheron, C., Recanati, A. and Rahn, M. (2017) Possible influence of alpha recoil track percolation on helium diffusivity in apatite, Goldschmidt Abstracts. Geochemical Society, Paris, France, p. 1983.

Ketcham, R.A., Guenthner, W.R. and Reiners, P.W. (2013) Geometric analysis of radiation damage connectivity in in zircon, and its implications for helium diffusion. American mineralogist 98, 350-360.

Kohn, B.P., Gleadow, A.J., Brown, R.W., Gallagher, K., Lorencak, M. and Noble, W.P. (2005) Visualizing thermotectonic and denudation histories using apatite fission track thermochronology, in: Reiners, P.W., Ehlers, T.A. (Eds.), Reviews in Mineralogy and Geochemistry. Mineralogical Society of America Geochemical Society, Chantilly, Virginia, pp. 527-565.

Kohn, B.P., Lorencak, M., Gleadow, A.J., Kohlmann, F., Raza, A., Osadetz, K.G. and Sorjonen-Ward, P. (2009) A reappraisal of low-temperature thermochronology of the eastern Fennoscandia Shield and radiation-enhanced apatite fission-track annealing. Geological Society, London, Special Publications 324, 193-216.

Larson, S.Å., Cederbom, C.E., Tullborg, E.-L. and Stiberg, J.-P. (2006) Comment on "Apatite fission track and (U–Th)/He data from Fennoscandia: An example of underestimation of fission track annealing in apatite" by Hendriks and Redfield [Earth Planet. Sci. Lett. 236 (443–458)]. Earth and Planetary Science Letters 248, 561-568.

Lavoie, D., Pinet, N., Dietrich, J., Zhang, S., Hu, K., Asselin, E., Chen, Z., Bertrand, R., Galloway, J. and Decker, V. (2013) Geological framework, basin evolution, hydrocarbon system data and conceptual hydrocarbon plays for the Hudson Bay and Foxe basins, Canadian Arctic. Geological Survey of Canada, Open File Report 7363, 213.

Li, W., Shen, Y., Zhou, Y., Nan, S., Chen, C.-H. and Ewing, R.C. (2017) In situ TEM observation of alpha-particle induced annealing of radiation damage in Durango apatite. Scientific reports 7, 14108.

Li, W., Wang, L., Lang, M., Trautmann, C. and Ewing, R.C. (2011) Thermal annealing mechanisms of latent fission tracks: Apatite vs. zircon. Earth and Planetary Science Letters 302, 227-235.

Li, W., Wang, L., Sun, K., Lang, M., Trautmann, C. and Ewing, R.C. (2010) Porous fission fragment tracks in fluorapatite. Physical Review B 82, 144109.

Liu, J., Glasmacher, U., Lang, M., Trautmann, C., Voss, K.-O., Neumann, R., Wagner, G. and Miletich, R. (2008) Raman spectroscopy of apatite irradiated with swift heavy ions with and without simultaneous exertion of high pressure. Applied Physics A 91, 17-22.

Lumpkin, G.R., Eby, R.K. and Ewing, R.C. (1991) Alpha-recoil damage in titanite (CaTiSiO 5): Direct observation and annealing study using high resolution transmission electron microscopy. Journal of Materials Research 6, 560-564.

Luo, Y., Hughes, J.M., Rakavan, J. and Pan, Y. (2009) Site preference of U and Th in Cl, F, and Sr apatites. American mineralogist 94, 345-351.

McCracken, A.D., Armstrong, D.K. and Bolton, T.E. (2000) Conodonts and corals in kimberlite xenoliths confirm a Devonian seaway in central Ontario and Quebec. Canadian Journal of Earth Sciences 37, 1651-1663.

[dataset] McDannell, K.T., Schneider, D.A., Zeitler, P.K., O'Sullivan, P.B. and Issler, D.R. (2018a) LA-ICP-MS apatite fission track and U-Pb dataset for southern Baffin Island, Nunavut, Canada. Interdisciplinary Earth Data Alliance (IEDA). doi: 10.1594/IEDA/111241.

McDannell, K.T., Schneider, D.A., Zeitler, P.K., O'Sullivan, P.B. and Issler, D.R. (2019) Reconstructing deep-time histories from integrated thermochronology: An example from southern Baffin Island, Canada. Terra Nova 31, 1-21.
McDannell, K.T., Zeitler, P.K., Janes, D.G., Idleman, B.D. and Fayon, A.K. (2018b) Screening apatites for (U-Th)/He thermochronometry via continuous ramped heating: He age components and implications for age dispersion. Geochimica et Cosmochimica Acta 223, 90-106.
McKeon, R.E. (2012) Apatite U-Th/He Thermochronometry in Slowly Eroding Landscapes: Addressing Age Dispersion to Understand Appalachian Topographic Development, Earth and Environmental Sciences. Lehigh University.
Miall, A.D. and Blakey, R.C. (2008) The Phanerozoic tectonic and sedimentary evolution of North America. Sedimentary basins of the world 5, 1-29.
Miro, S., Costantini, J., Haussy, J., Chateigner, D. and Balanzat, E. (2012) Damage and helium migration induced in fluorapatite sinters by swift heavy ion irradiations. Journal of nuclear materials 423, 120-126.
Miro, S., Grebille, D., Chateigner, D., Pelloquin, D., Stoquert, J.-P., Grob, J.-J., Costantini, J.-M. and Studer, F. (2005) X-ray diffraction study of damage induced by swift heavy ion irradiation in fluorapatite. Nuclear Instruments and Methods in Physics Research Section B: Beam Interactions with Materials and Atoms 227, 306-318.
Murakami, T., Chakoumakos, B.C., Ewing, R.C., Lumpkin, G.R. and Weber, W.J. (1991) Alpha-decay event damage in zircon. American mineralogist 76, l5l0-1532.
Morehead Jr, F. and Crowder, B. (1970) A model for the formation of amorphous Si by ion bombardment. Radiation Effects 6, 27-32.
Nadzri, A., Schauries, D., Mota-Santiago, P., Trautmann, C., Gleadow, A.J.W., Hawley, A. and Kluth, P. (2017) Composition and orientation dependent annealing of ion tracks in apatite - Implications for fission track thermochronology. Chemical Geology 451, 9-16.
Naeser, C. and Faul, H. (1969) Fission track annealing in apatite and sphene. Journal of Geophysical Research 74, 705-710.
Nasdala, L., Hanchar, J.M., Kronz, A. and Whitehouse, M.J. (2005) Long-term stability of alpha particle damage in natural zircon. Chemical Geology 220, 83-103.
Nasdala, L., Wenzel, M., Vavra, G., Irmer, G., Wenzel, T. and Kober, B. (2001) Metamictisation of natural zircon: accumulation versus thermal annealing of radioactivity-induced damage. Contrib. Miner. Petrol. 141, 125-144.
Nassichuk, W. and McIntyre, D. (1995) Cretaceous and Tertiary fossils discovered in kimberlites at Lac de Gras in the Slave Province, Northwest Territories. Geological Survey of Canada Current Research 1995, 109-114.
O'Sullivan, P.B. and Parrish, R.R. (1995) The importance of apatite composition and single-grain ages when interpreting fission track data from plutonic rocks: a case study from the Coast Ranges, British Columbia. Earth and Planetary Science Letters 132, 213-224.
Ouchani, S., Dran, J.-C. and Chaumont, J. (1997) Evidence of ionization annealing upon helium-ion irradiation of pre-damaged fluorapatite. Nuclear Instruments and Methods in Physics Research Section B: Beam Interactions with Materials and Atoms 132, 447-451.
Pan, Y. and Fleet, M.E. (2002) Compositions of the apatite-group minerals: substitution mechanisms and controlling factors. Reviews in Mineralogy and Geochemistry 48, 13-49.

1269 Partin, C., Bekker, A., Corrigan, D., Modeland, S., Francis, D. and Davis, D. (2014)
1270 Sedimentological and geochemical basin analysis of the Paleoproterozoic Penrhyn and
1271 Piling groups of Arctic Canada. Precambrian Research 251, 80-101.
1272 Percival, J., McNicoll, V., Brown, J. and Whalen, J. (2004) Convergent margin tectonics, central
1273 Wabigoon subprovince, Superior Province, Canada. Precambrian Research 132, 213-244.
1274 Percival, J., Skulski, T., Sanborn-Barrie, M., Stott, G., Leclair, A., Corkery, M. and Boily, M.
1275 (2012) Geology and tectonic evolution of the Superior Province, Canada. Tectonic Styles
1276 in Canada: The Lithoprobe Perspective. Geol Assoc Canada Spec Paper 49, 321-378.
1277 Petit, J.-C., Langevin, Y. and Dran, J.-C. (1985) Radiation-enhanced release of uranium from
1278 accessory minerals in crystalline rocks. Geochimica et Cosmochimica Acta 49, 871-876.
1279 Pinet, N., Kohn, B. and Lavoie, D. (2016) The ups and downs of the Canadian Shield: 1-
1280 preliminary results of apatite fission track analysis from Hudson Bay region. Geological
1281 Survey of Canada, p. 59.
1282 Pinet, N., Lavoie, D., Dietrich, J., Hu, K. and Keating, P. (2013) Architecture and subsidence
1283 history of the intracratonic Hudson Bay Basin, northern Canada. Earth-Science Reviews
1284 125, 1-23.
1285 Powell, J., Schneider, D.A., Desrochers, A., Flowers, R.M., Metcalf, J., Gaidies, F. and Stockli,
1286 D.F. (2018a) Low-temperature thermochronology of Anticosti Island: a case study on the
1287 application of conodont (U-Th)/He thermochronology to carbonate basin analysis.
1288 Marine and Petroleum Geology.
1289 Powell, J.W., Schneider, D.A. and Issler, D.R. (2018b) Application of multi- kinetic apatite
1290 fission track and (U- Th)/He thermochronology to source rock thermal history: a case
1291 study from the Mackenzie Plain, NWT, Canada. Basin Research 30, 497-512.
1292 Price, P. and Walker, R. (1963) Fossil tracks of charged particles in mica and the age of
1293 minerals. Journal of Geophysical Research 68, 4847-4862.
1294 R Core Team (2018) R: A language and environment for statistical computing. R Foundation for
1295 Statistical Computing, Vienna, Austria. URL https://www.R-project.org/.
1296 Rabone, J., Carter, A., Hurford, A. and de Leeuw, N.H. (2008) Modelling the formation of
1297 fission tracks in apatite minerals using molecular dynamics simulations. Physics and
1298 Chemistry of Minerals 35, 583-596.
1299 Ravenhurst, C.E., Roden-Tice, M.K. and Miller, D.S. (2003) Thermal annealing of fission tracks
1300 in fluorapatite, chlorapatite, manganoapatite, and Durango apatite: Experimental results.
1301 Canadian Journal of Earth Sciences 40, 995-1007.
1302 Rayner, N., Chakungal, J. and Sanborn-Barrie, M. (2011) New U-Pb geochronological results
1303 from plutonic and sedimentary rocks of Southampton Island, Nunavut. Geological Survey
1304 of Canada.
1305 Recanati, A., Gautheron, C., Barbarand, J., Missenard, Y., Pinna-Jamme, R., Tassan-Got, L.,
1306 Carter, A., Douville, É., Bordier, L. and Pagel, M. (2017) Helium trapping in apatite
1307 damage: Insights from (U-Th-Sm)/He dating of different granitoid lithologies. Chemical
1308 Geology 470, 116-131.
1309 Ritter, W. and Märk, T. (1986) Radiation damage and its annealing in apatite. Nuclear
1310 Instruments and Methods in Physics Research Section B: Beam Interactions with
1311 Materials and Atoms 14, 314-322.
1312 Rodríguez, M.P., Charrier, R., Brichau, S., Carretier, S., Farías, M., de Parseval, P. and Ketcham,
1313 R.A. (2018) Latitudinal and Longitudinal Patterns of Exhumation in the Andes of
1314 North- Central Chile. Tectonics 37, 2863-2886.

Schneider, D.A. and Issler, D.R. (2019) Application of low-temperature thermochronology to hydrocarbon exploration, in: Malusa, M.G., Fitzgerald, P. (Eds.), Fission-Track Thermochronology and its Application to Geology, 1 ed. Springer International Publishing, New York, p. 676.

Seiler, C., Gleadow, A. and Kohn, B. (2013) Apatite fission track dating by LA-ICP-MS and External Detector Method: How do they stack up?, AGU Fall Meeting abstracts.

Seydoux-Guillaume, A.-M., Deschanels, X., Baumier, C.d., Neumeier, S., Weber, W.J. and Peuget, S. (2018) Why natural monazite never becomes amorphous: experimental evidence for alpha self-healing. American mineralogist 10.2138./am-2018-6447.

Shuster, D.L. and Farley, K.A. (2009) The influence of artificial radiation damage and thermal annealing on helium diffusion kinetics in apatite. Geochimica et Cosmochimica Acta 73, 6183-6196.

Shuster, D.L., Flowers, R.M. and Farley, K.A. (2006) The influence of natural radiation damage on helium diffusion kinetics in apatite. Earth and Planetary Science Letters 249, 148-161.

Stasiuk, L.D., Sweet, A.R. and Issler, D.R. (2006) Reconstruction of burial history of eroded Mesozoic strata using kimberlite shale xenoliths, volcaniclastic and crater facies, Northwest Territories, Canada. International Journal of Coal Geology 65, 129-145.

Timms, N.E., Kinny, P.D. and Reddy, S.M. (2006) Enhanced diffusion of Uranium and Thorium linked to crystal plasticity in zircon. Geochemical Transactions 7, 1-16.

Vermeesch, P. (2012) On the visualisation of detrital age distributions. Chemical Geology 312, 190-194.

Vermeesch, P. (2017) Statistics for LA-ICP-MS based fission track dating. Chemical Geology 456, 19-27.

Wagner, G. (1968) Fission track dating of apatites. Earth and Planetary Science Letters 4, 411-415.

Wang, L., Cameron, M., Weber, W., Crowley, K. and Ewing, R. (1994) In situ TEM observation of radiation induced amorphization of crystals with apatite structure. Hydroxyapatite and Related Materials. PW Brown and B. Constantz (eds) CRC Press, London, 243-249.

Weber, W.J., Duffy, D.M., Thomé, L. and Zhang, Y. (2015) The role of electronic energy loss in ion beam modification of materials. Current Opinion in Solid State and Materials Science 19, 1-11.

Weber, W., Ewing, R. and Meldrum, A. (1997) The kinetics of alpha-decay-induced amorphization in zircon and apatite containing weapons-grade plutonium or other actinides. Journal of nuclear materials 250, 147-155.

Weber, W.J. and Matzke, H.J. (1986) Radiation effects in actinide host phases. Radiation Effects 98, 93-99.

Weber, W.J., Zhang, Y., Xiao, H. and Wang, L. (2012) Dynamic recovery in silicate-apatite structures under irradiation and implications for long-term immobilization of actinides. RSC Advances 2, 595-604.

Wei, T. and Simko, V. (2017) R package "corrplot": Visualization of a Correlation Matrix (Version 0.84). Available from https://github.com/taiyun/corrplot.

Weikusat, C., Glasmacher, U.A., Schuster, B., Trautmann, C., Miletich, R. and Neumann, R. (2011) Raman study of apatite amorphised with swift heavy ions under various irradiation conditions. Physics and Chemistry of Minerals 38, 293-303.

Wessel, P., Smith, W.H., Scharroo, R., Luis, J. and Wobbe, F. (2013) Generic mapping tools: improved version released. Eos, Transactions American Geophysical Union 94, 409-410.

Whitmeyer, S.J. and Karlstrom, K.E. (2007) Tectonic model for the Proterozoic growth of North America. Geosphere 3, 220-259.
Willett, C.D., Fox, M. and Shuster, D.L. (2017) A helium-based model for the effects of radiation damage annealing on helium diffusion kinetics in apatite. Earth and Planetary Science Letters 477, 195-204.
Zeitler, P.K., Enkelmann, E., Thomas, J.B., Watson, E.B., Ancuta, L.D. and Idleman, B.D. (2017) Solubility and trapping of helium in apatite. Geochimica et Cosmochimica Acta 209, 1-8.
Zhang, S. and Pell, J. (2014) Conodonts recovered from the carbonate xenoliths in the kimberlites confirm the Paleozoic cover on the Hall Peninsula, Nunavut. Canadian Journal of Earth Sciences 51, 142-155.
Zhang, Y., Sachan, R., Pakarinen, O.H., Chisholm, M.F., Liu, P., Xue, H. and Weber, W.J. (2015) Ionization-induced annealing of pre-existing defects in silicon carbide. Nature Communications 6:8049, 1-6. doi: 10.1038/ncomms9049

FIGURE CAPTIONS

Figure 1. Map of the Canadian Shield with simplified geologic domains modified from Whitmeyer and Karlstrom (2007). Bedrock AFT samples are shown as circles with their corresponding central age, red points are LA-ICP-MS AFT samples and the orange point is the published Pinet et. al. (2016) sample. Areas in purple show Paleozoic succession of Hudson Bay, sub-basins, and surrounding Arctic platform, which imply bedrock has been at or near the present surface since (at least) the Ordovician. Refer to table 1 and text in section 4 for more information on AFT samples. Missing section in central Hudson Bay is younger overlying Mesozoic-Cenozoic sediment. Quebec Grenvillian and Cumberland Peninsula, Baffin Island samples are shown and discussed for comparison only, as they have a more complex thermal history compared to the Canadian Shield samples. Sample ID shown in box near central age value for each sample, refer to table 1. THO = Trans-Hudson Orogen; GSL = Great Slave Lake shear zone; STZ = Snowbird Tectonic Zone; CP = Cumberland Peninsula; HP = Hall Peninsula; AB = Athabasca Basin; TB = Thelon Basin.

Figure 2. (A) Conventional plot of eU content versus AFT age as well as mean track length for all bedrock samples. Other than the two high eU examples there is a decrease in age with eU across all samples. A simple least-squares linear regression (removing the two eU outliers) produces an R^2 value of 0.36. (B) Highest eU grains clearly have the shortest MTL, however there are not enough intermediate-to-high eU data to confidently extrapolate the relationship. (C) All single grains shown in F and Cl weight percent. Barbarand et al., (2003) demonstrate Cl does not dominate the apatite structure (retentivity) until >~0.35 wt. % or >0.1 apfu. Our dataset is dominated by F-apatite and/or hydroxyl-bearing F-apatite varieties.

Figure 3. Radial plots (log transformed) from DensityPlotter v. 8.2 for LA-ICP-MS AFT data. "Open jaw" radial plots are typical of our dataset and are generally interpreted as meaning that there is a complex mixture of AFT ages that are non-Poissonian in character. Refer to table 1 for sample information. As an example of single-grain age dispersion effects, we have shown the two-component mixture model ages associated with age peaks of ca. 160 and ca. 75 Ma for sample 09SRB-M100. This illustrates how the central age for a sample can be misleading in cases of high dispersion. For sample 14SUB-H43A the opposite is true as this sample only has 10% age dispersion and lower *n*. Stars denote published samples from Pinet et al. (2016) and Powell et al., (2018a).

Figure 4. Fission track length distributions for each sample shown in figure 3. Length distributions are presented as frequency (%) in 1 μm bins with equivalent normal distributions shown for the mean ± 1σ (solid, blue curve) and the mode (dashed, red curve). A mismatch between the equivalent normal distributions is taken to suggest bimodality and more complex, episodic thermal histories.

Figure 5. Bedrock sample AFT age versus eU and eCl for each sample in Table 1. Notice that each sample has a negative age-eU trend for single grains, only sample 12NK-L18A3 does not and this is discussed in section 5. There is no clear age relationship with eCl (r_{mr0}). Note: samples are coloured the same in figure 5 and figure 9. In the few cases where a grain was not probed, we used the average sample eCl value as a placeholder.

Figure 6. Examples of the relationship between eU and AFT age, eCl, and r_{mr0}. (A) The Baffin Island sample exhibits behaviour indicative of Cl or another element controlling retentivity (> than any eU effect), whereas the other samples suggest eU is controlling retentivity (B-C). The panels in C are age-normalized to show both samples PBA-98-743 and 03-GRS-013 together. Unfilled circles are values outside the color ramp maximum. Trend lines (reduced major axis regression) are for visual purposes only, to highlight the spurious correlation (upper panel) and the lack of correlation (dashed, middle panel)

between eU and eCl (or r_{mr0}). The color ramp change from red to blue is arbitrarily chosen to be the approximate mean eCl value of all the grains. Panels D-F: Scatter plots of other Canadian Shield AFT examples. (D) An example from Pinet et al. (2016) showing the relationship between ^{238}U and age. The relation is similar to our data except not as well defined given that there are a low number of grains dated and eU was not calculated, and eCl values are all similar and negative suggesting end-member apatite composition. (E) Sample 09SRB-M100C1 from Baffin Island shows a spurious relationship between AFT age and kinetic parameters eU and eCl/r_{mr0} (discussed in text, shown in fig. 6A) that is not readily apparent when eCl is plotted against AFT age shown here. This sample also underwent episodic thermal annealing. (F) Sample 14SUB-H43A also from Baffin Island displays lower eU variability than most samples and all single grains are in a range of "typical apatite" eU, it also has characteristic highly clustered positive eCl values suggesting low kinetic variability between grains. This relationship results in the appearance of less age variability, which may be naturally inherent to the sample or a result of unintended grain selection preference.

Figure 7. Correlation matrices for standardized EPMA compositional analyses. Analyses are for Cl, eU, F, Fe, Mg, Mn, Na, S, Sr, and REE (Ce, La, Y) in wt. % shown in hierarchical clustering of correlation coefficients and (B and D) only show correlations with p-values <0.05 or at the 95% confidence level. Positive (+1, black) or negative (anti-) correlation (-1, white) is shown with the size of the corresponding circle equal to the linear correlation coefficient (i.e. small circle is low correlation coefficient and *vice versa*). Notice the anti-correlation between F and Cl as expected. (A, B) Examples are shown for the Superior Province sample PBA-98-743 that displays eU variability in relation with single-grain AFT age (fig. 3 and fig. 5) versus sample 12NK-L18A3 with very high eU (>>100 ppm) and no obvious age-eU relationship (D). Note that care is required during interpretation of these relationships, as some grains may seem highly correlated but are represented by only a few EPMA analyses/grains, where the majority of grains are zero/below detection limit, which is typically the case for REE, seen in panel C plots of normalized eU, Ce, and La for sample PBA-98-743. Best-fit linear trend (black line) and correlation coefficient (r) are shown for each plot in C. The SI document shows correlation coefficients for each AFT sample (table S1) and correlation matrices for each sample (fig. S1).

Figure 8. Example of both AFT and AHe data from Melville Peninsula with respect to α-dose from Pinet et al., (2016). **(A)** AFT (sample 09SZ-23-01; circles) and AHe ages (samples 09SZ23-01 and 09SZ24-01; hexagons) with respect to eU. The measured ^{238}U value is used as a proxy for eU here. This is a good approximation because most accompanying AHe single grains have low Th, <10 ppm. **(B)** AFT and AHe ages plotted against the estimated α-dose. The AFT data are older vintage without U-Pb ages; therefore we used the t_{EDA} from nearby AFT sample 10CXAD-086. **(C-D)** The same plot as A and B, but for sample 13JP10 on Anticosti Island (Powell et al., 2018a). There is no clear relationship between age and eU for this sample.

Figure 9. Plot of estimated α-dose vs. age for selected Canadian Shield AFT samples summarized in table 1 and shown on fig. 1. Samples with long t_{EDA} plot at high damage levels above the threshold and show negative age-α-dose correlations, whereas samples with shorter t_{EDA} show the expected positive relationship at low damage below the percolation threshold. Collectively these samples capture the full range in α-dose or damage level for our dataset. 13LVA04 and 12NK-L18A3 demonstrate the effect of low/high eU variance (σ^2) on α-dose. Black dashed line is the percolation threshold from Ketcham et al., (2017). Lower panel: estimated α-dose from young samples taken from published literature. All grains fall below the ^{238}U damage percolation threshold, implying no significant damage effects on AFT age. Sample 13JP10 shown on both plots for reference. Single-grain age errors not shown on plots for clarity but AFT age percent error range (1σ) for each sample is shown beside the sample ID. Note: Wrangellia sample plots off of scale at low α-dose.

Figure 10: An example of visualizing multi-kinetic samples in terms of composition and radiation damage for thermal history modeling. Panels are read vertically for each sample. **(A, E)** Samples 02NKL-

871 from Quebec and 11CXAN017 from Melville Peninsula are characterized by high dispersion and fail the X^2 test. Radial plots show age populations based solely on mixture modeling. Note that age peak 1 for 11CXAN017 contains noticeably higher precision grains (i.e. high eU). **(B, F)** AFT age plotted against eCl for each sample. Points are colors by their respective age population shown in the radial plot panels. **(C, G)** AFT ages are colored by eCl (same scale for each sample) and plotted against α-dose. There is complete compositional overlap between populations. **(D, H)** The same plots as C and G only here the age populations are instead colored by their respective age populations identified in the radial plot mixture models. Note that grains of similar age (in D) fall above and below the ^{238}U α-recoil percolation threshold (dashed black line).

Table 1. Summary of apatite fission track results from across the Canadian Shield (see fig. 1 for locations). All U measurements used for age calculations were obtained by LA-ICP-MS analysis. All of our samples fail the X^2 test. Percent difference between the central and pooled age is shown. Single-grain age span between the oldest/youngest grains (not including error) shows the AFT heterogeneity within samples and eU range is given with the mean eU in brackets. Sample 03-GRS-013 has a single anomalously old grain, which refers to the age span value in brackets. Refer to text for discussion of results. Note: some single grains within samples were unable to be probed or do not have chemical data, therefore an effective Cl/r_{mr0} value was unable to be calculated for those grains, in these instances the average respective kinetic parameter value for the entire dataset was used for plotting purposes. See SI for full AFT dataset.

Table 2. Pearson correlation coefficients for all Canadian Shield samples where eU correlated with other elemental data. All samples are shown in the SI with the ranked r-values for the top 20 elemental pairs for each sample.

Table 1. *Apatite fission track results for the Canadian Shield*

Sample	GSC Lab #	Rock Type	Long. DD	Lat. DD	no. age gr.	grain age span (My)	Pooled Age (Ma)	1σ (Ma)	Central Age (Ma)	1σ (Ma)	% diff	MTL (µm)	1σ (µm)	track count	avg. D_{par} (µm)	avg. eU (ppm)	avg. r_{mr0}	avg. Cl (apfu)	Eff. Cl (apfu)	U-Pb age pop. (Ma)	2σ (Ma)
Western Superior Province, Ontario																					
PBA-98-743	5479	tonalite	-90.12120	49.92996	40	1233	572	16	597	37	4	12.07	1.94	130	1.89	1-19 [7]	0.84	0.008	0.002	2971	174
03-GRS-013	8105	tonalite qtz. diorite	-87.89872	53.66566	40	715 [2119]	414	14	447	34	8	12.51	1.63	131	1.91	1-241 [33]	0.84	0.003	-0.005	3009	94
Slave Province, Northwest Territories																					
BNB97-035	8460	biotite granitoid	-112.9215	63.23258	40	495	229	22	272	16	17	12.75	1.80	116	1.72	0.2-98 [21]	0.85	0.006	-0.041	2858	124
12-DRA03-001	8313	plag. porph. intrusive	-114.8500	63.33333	40	378	336	11	344	14	2	12.04	2.39	131	1.87	2-55 [16]	0.83	0.019	0.023	2628	96
12NK-L18A3	10889	granitic gneiss	-102.0765	66.14816	26	236	392	9	397	13	1	11.91	2.06	78	1.85	139-655 [339]	0.79	0.012	0.135	1788	40
Churchill-Rae Province, Melville Peninsula region, Nunavut																					
SNB-01-M2055	7271	foliated tonalite	-91.11273	66.87706	30	482	349	10	356	18	2	12.19	2.30	130	2.00	0.2-46 [14]	0.84	0.003	0.002	1940	68
10CXAD-086A	10313	gabbro-anorthosite	-82.05779	67.82549	40	1832	363	28	460	44	24	12.60	1.79	132	2.12	0.2-73 [13]	0.82	0.029	0.059	1803	73
11CXAN017	10697	Bt Kfs monzogranite	-84.79986	67.75710	18	578	418	11	452	31	8	12.67	1.92	120	1.95	3-43 [21]	0.85	0.002	-0.022	1676	59
13LVA04	11068	gabbro	-101.7240	62.69358	40	739	546	34	557	31	2	12.44	2.06	121	1.92	3-42 [7]	0.80	0.012	0.097	2224	125
09SZ-23-01*	N/A	granitic gneiss	-82.84220	69.49660	19	406	463	30	486	27	5	12.18	1.58	100	1.67	11-20 [14]**	0.85	0.016	-0.043	-	-
Churchill-Rae Province, Southampton Island, Nunavut																					
07CYA-M38B	9422	gabbroic anorthosite	-83.60701	64.84525	40	595	342	10	384	21	12	12.22	2.00	132	1.90	1-71 [22]	0.84	0.024	0.007	1834	60
07CYA-M133A	9558	diorite	-81.90056	64.54453	15	357	364	11	375	17	3	11.57	2.16	101	2.26	7-258 [74]	0.80	0.086	0.098	1812	79
Rae craton, southern Baffin Island, Nunavut																					
09SRB-M100	10840	semipelite	-64.48663	65.46074	35	222	97	4	102	8	5	12.94	2.23	41	2.14	1-69 [22]	0.83	0.023	0.041	1674	35
14SUB-H43A	11261	gt-bt psammite	-66.91792	64.56119	25	256	440	11	442	12	0.5	12.46	1.72	130	2.29	16-35 [26]	0.82	0.022	0.045	1782	38
Grenville Province, Quebec																					
02NKL-871	7626	granitic orthogneiss	-62.64094	50.26647	35	540	161	5	177	13	9	12.27	1.80	135	1.83	2-160 [31]	0.85	0.008	-0.018	951	38
13JP10*	N/A	Grenv. basement	see Powell et al., 2018		40	135	123	4	126	4	2	12.37	1.64	171	2.01	5-68 [29]	0.83	0.174	0.038	931	38

*Samples from Pinet et al. (2016) and Powell et al., 2018a, respectively

**Calculated by uniformly applying associated single-grain (U-Th)/He average Th and Sm concentrations with each AFT ^{238}U measurement to give a more representative value for the eU content.

1516

1517

Table 2: Pearson correlation coefficients (r-values) for eU with respect to other EPMA data

PBA-98-743			03GRS013			BNB97-035			12-DRA03-001			12NK-L18A3			SNB-01-M2055			10CXAD-086A			11CXAN017			07CYA-M38B			07CYA-M133A			09SRBM100			14SUB-H43A			02-NKL-871		
eU	Ce	0.68	eU	Ce	0.71	eU	Cl	0.30	eU	Na	-0.34	eU	La	0.50	eU	Mg	-0.43	eU	Y	0.41	eU	Y	0.69	eU	Na	0.44	eU	Y	0.58	eU	Fe	0.68	eU	Ce	0.40	eU	Y	0.63
eU	La	0.56	eU	Y	0.51							eU	Ce	0.48	eU	F	-0.37				eU	Mg	0.39	eU	Fe	-0.37	eU	Na	-0.57	eU	Mn	0.61				eU	Ce	0.36
eU	Cl	0.50	eU	S	0.48							eU	Fe	0.41	eU	OH	0.36				eU	S	0.34	eU	Y	0.26	eU	La	0.48							eU	S	-0.34
eU	Y	0.46	eU	F	-0.42										eU	Fe	0.30				eU	Ce	0.33													eU	Sr	0.29
eU	Mn	0.45	eU	OH	0.42																eU	Sr	0.33														
eU	F	-0.41	eU	La	0.39																eU	Cl	0.31														
eU	OH	0.40	eU	Mg	-0.33																																	

1518

Figure1

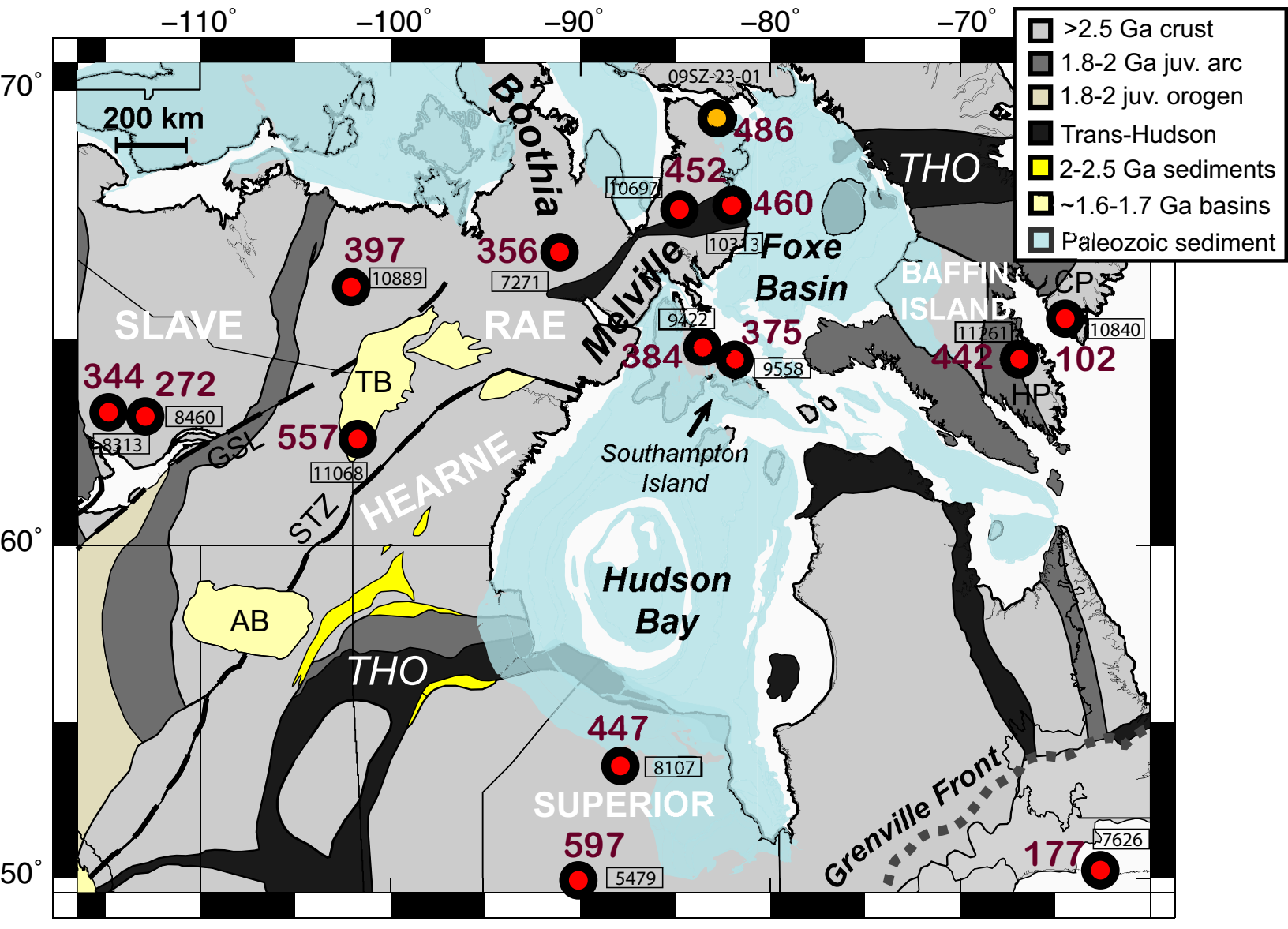
−110°
−100°
−90°
−80°
−70°
70°
60°
50°
200 km
>2.5 Ga crust
1.8-2 Ga juv. arc
1.8-2 juv. orogen
Trans-Hudson
2-2.5 Ga sediments
~1.6-1.7 Ga basins
Paleozoic sediment
Boothia
09SZ-23-01
486
452
10697
460
10343
THO
Foxe
Basin
Melville
397
10889
356
7271
SLAVE
RAE
9422
375
9558
384
BAFFIN
ISLAND
CP
11261
10840
442
102
HP
344
272
8460
8313
TB
GSL
557
11068
STZ
HEARNE
Southampton
Island
DO
Hudson
Bay
AB
THO
447
8107
SUPERIOR
597
5479
Grenville Front
177
7626

Figure2

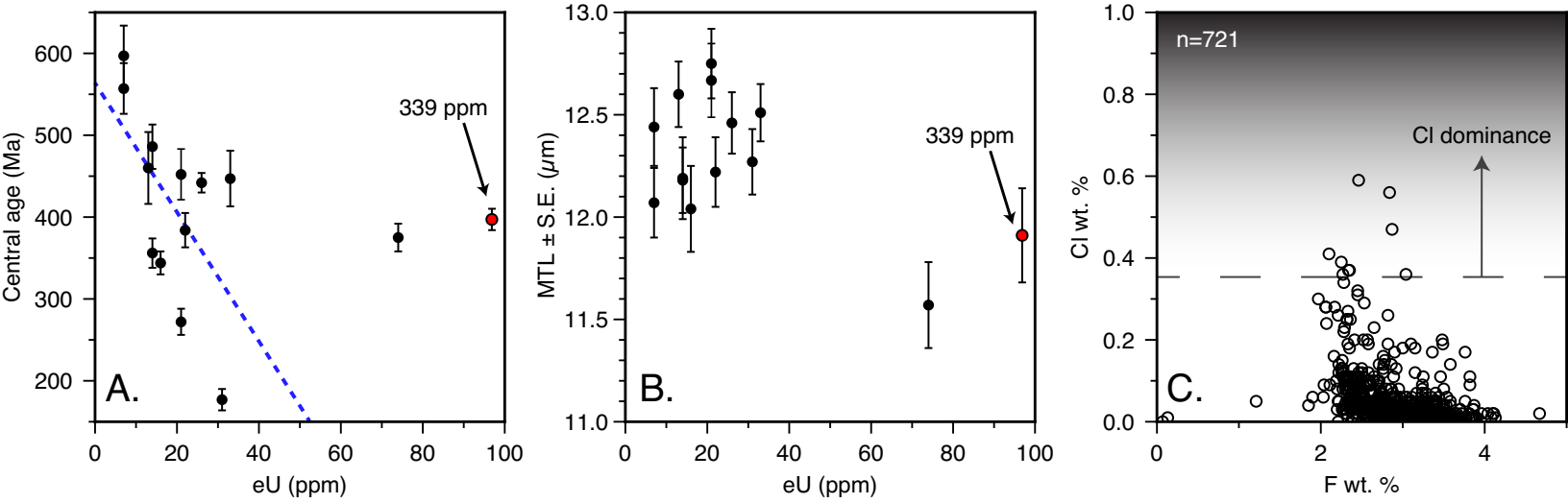
A.
Central age (Ma)
eU (ppm)
339 ppm
B.
MTL ± S.E. (μm)
eU (ppm)
339 ppm
C.
n=721
Cl dominance
Cl wt. %
F wt. %

Figure3

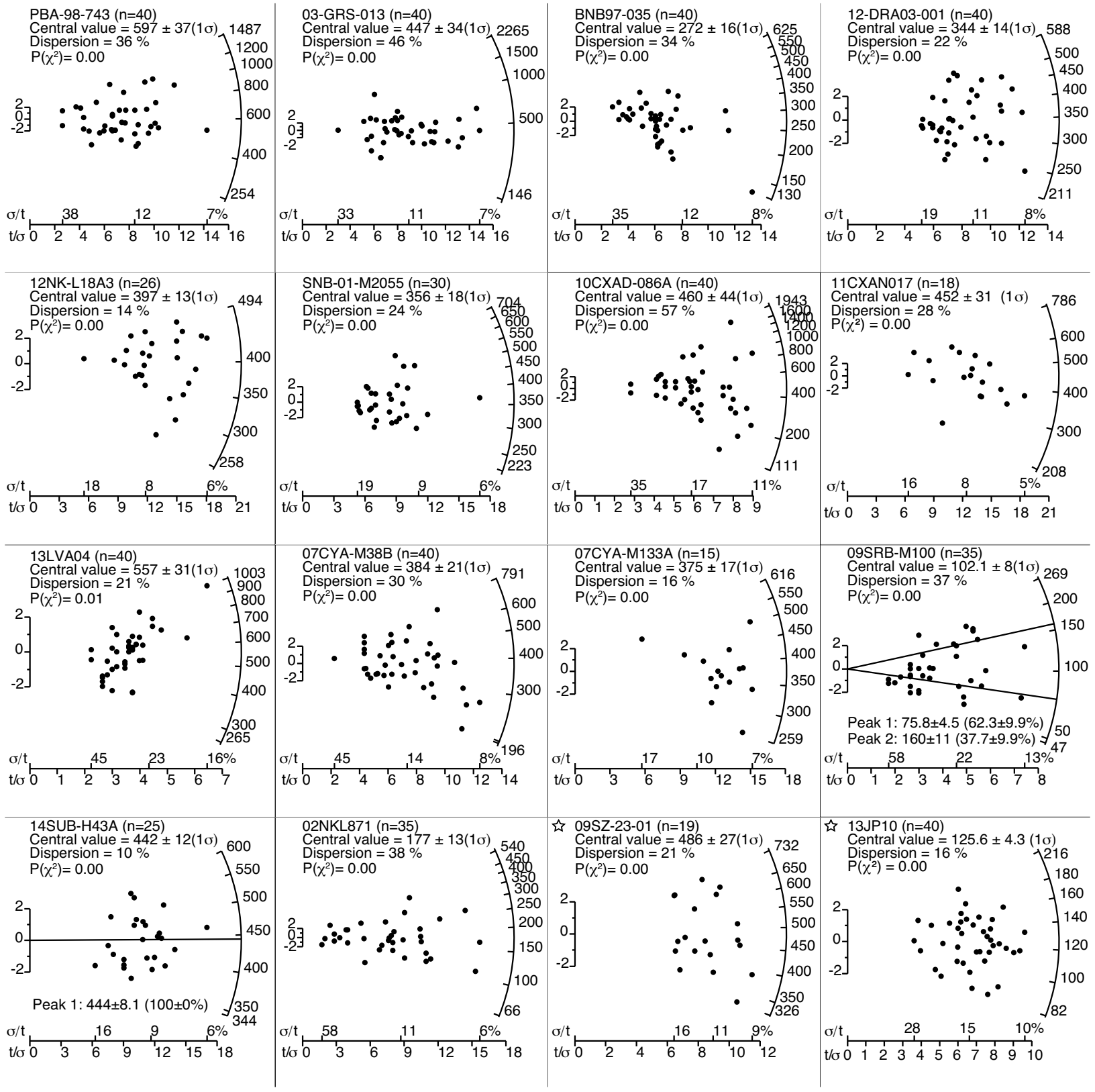
PBA-98-743 (n=40)
Central value = 597 ± 37(1σ)
Dispersion = 36 %
P(χ²)= 0.00
03-GRS-013 (n=40)
Central value = 447 ± 34(1σ)
Dispersion = 46 %
P(χ²)= 0.00
BNB97-035 (n=40)
Central value = 272 ± 16(1σ)
Dispersion = 34 %
P(χ²)= 0.00
12-DRA03-001 (n=40)
Central value = 344 ± 14(1σ)
Dispersion = 22 %
P(χ²)= 0.00
12NK-L18A3 (n=26)
Central value = 397 ± 13(1σ)
Dispersion = 14 %
P(χ²)= 0.00
SNB-01-M2055 (n=30)
Central value = 356 ± 18(1σ)
Dispersion = 24 %
P(χ²)= 0.00
10CXAD-086A (n=40)
Central value = 460 ± 44(1σ)
Dispersion = 57 %
P(χ²)= 0.00
11CXAN017 (n=18)
Central value = 452 ± 31 (1σ)
Dispersion = 28 %
P(χ²) = 0.00
13LVA04 (n=40)
Central value = 557 ± 31(1σ)
Dispersion = 21 %
P(χ²)= 0.01
07CYA-M38B (n=40)
Central value = 384 ± 21(1σ)
Dispersion = 30 %
P(χ²)= 0.00
07CYA-M133A (n=15)
Central value = 375 ± 17(1σ)
Dispersion = 16 %
P(χ²)= 0.00
09SRB-M100 (n=35)
Central value = 102.1 ± 8(1σ)
Dispersion = 37 %
P(χ²)= 0.00
Peak 1: 75.8±4.5 (62.3±9.9%)
Peak 2: 160±11 (37.7±9.9%)
14SUB-H43A (n=25)
Central value = 442 ± 12(1σ)
Dispersion = 10 %
P(χ²)= 0.00
Peak 1: 444±8.1 (100±0%)
02NKL871 (n=35)
Central value = 177 ± 13(1σ)
Dispersion = 38 %
P(χ²)= 0.00
☆ 09SZ-23-01 (n=19)
Central value = 486 ± 27(1σ)
Dispersion = 21 %
P(χ²)= 0.00
☆ 13JP10 (n=40)
Central value = 125.6 ± 4.3 (1σ)
Dispersion = 16 %
P(χ²) = 0.00
σ/t
t/σ

Figure4

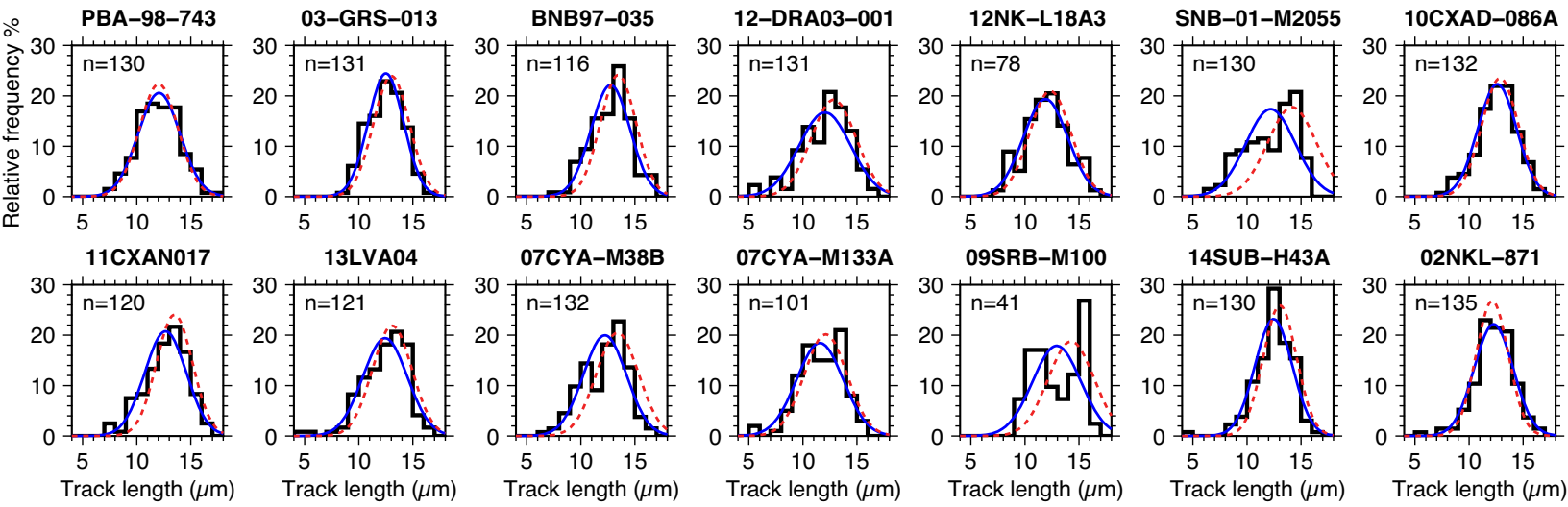
PBA–98–743
n=130
03–GRS–013
n=131
BNB97–035
n=116
12–DRA03–001
n=131
12NK–L18A3
n=78
SNB–01–M2055
n=130
10CXAD–086A
n=132
11CXAN017
n=120
13LVA04
n=121
07CYA–M38B
n=132
07CYA–M133A
n=101
09SRB–M100
n=41
14SUB–H43A
n=130
02NKL–871
n=135
Relative frequency %
Track length (μm)
0
10
20
30
5
10
15

Figure5

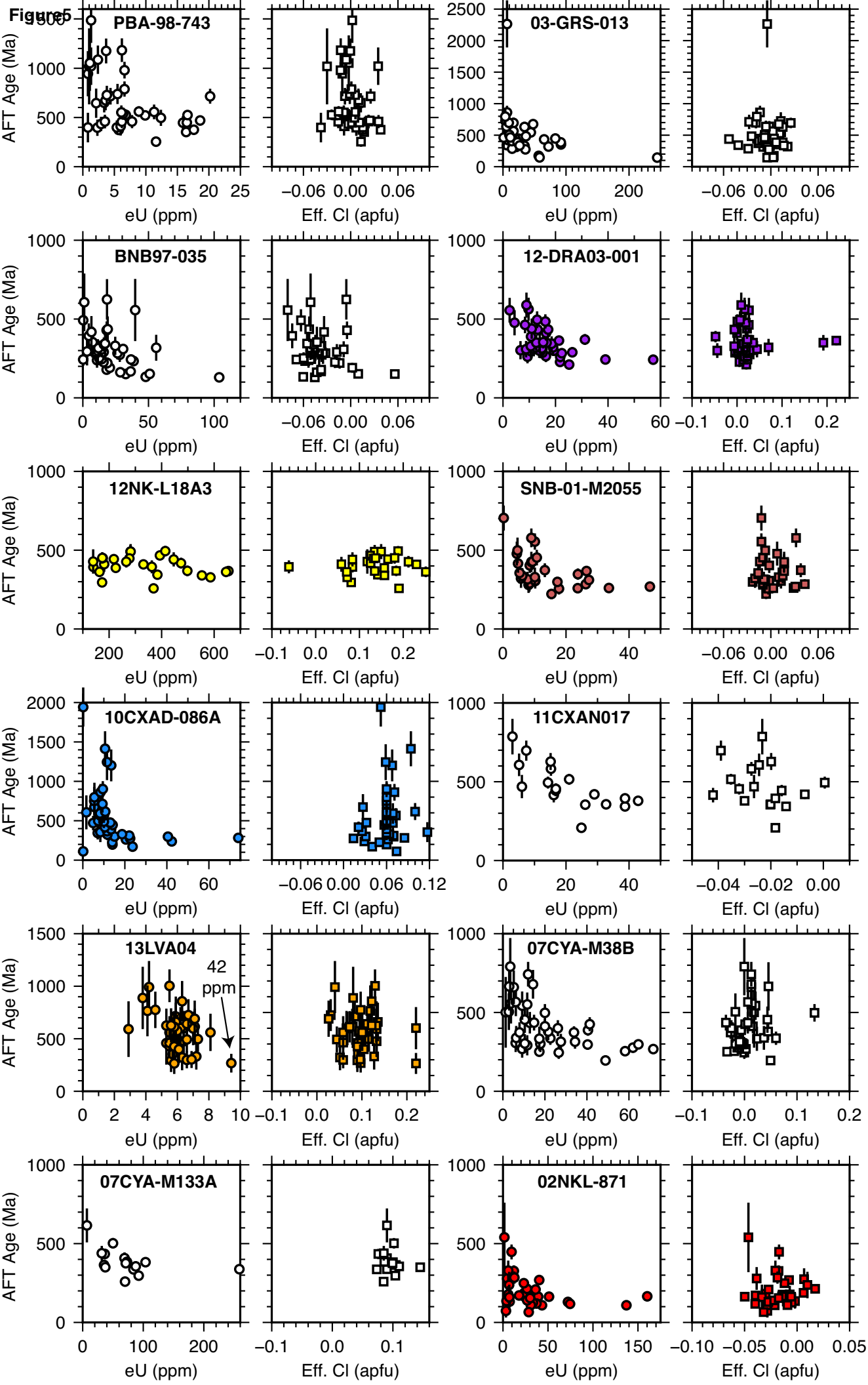
PBA-98-743
03-GRS-013
BNB97-035
12-DRA03-001
12NK-L18A3
SNB-01-M2055
10CXAD-086A
11CXAN017
13LVA04
42 ppm
07CYA-M38B
07CYA-M133A
02NKL-871
AFT Age (Ma)
eU (ppm)
Eff. Cl (apfu)

Figure6

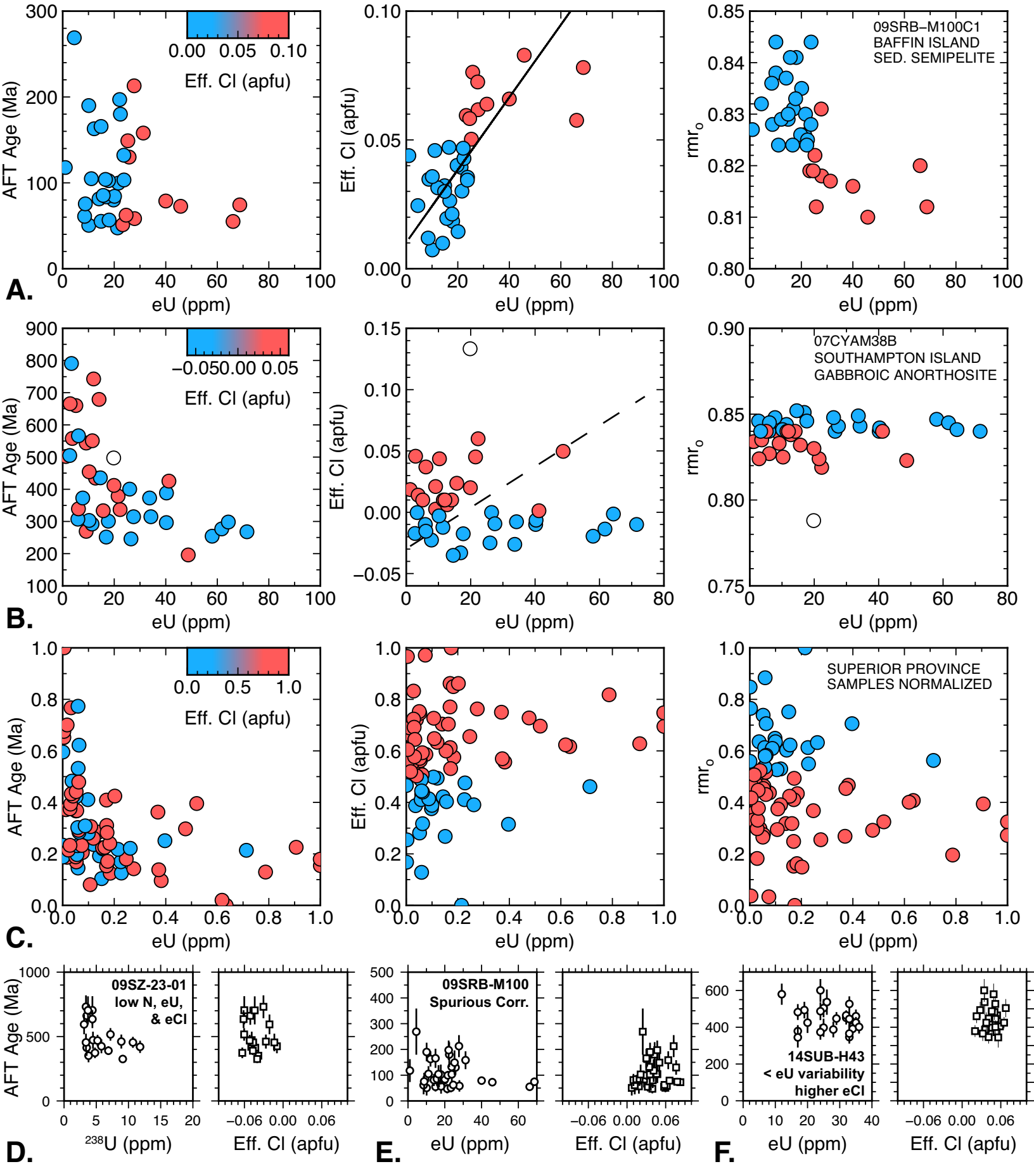
A.
AFT Age (Ma)
eU (ppm)
Eff. Cl (apfu)
0.00 0.05 0.10
Eff. Cl (apfu)
eU (ppm)
rmr$_o$
09SRB–M100C1
BAFFIN ISLAND
SED. SEMIPELITE
B.
AFT Age (Ma)
eU (ppm)
–0.050.00 0.05
Eff. Cl (apfu)
Eff. Cl (apfu)
eU (ppm)
rmr$_o$
07CYAM38B
SOUTHAMPTON ISLAND
GABBROIC ANORTHOSITE
C.
AFT Age (Ma)
eU (ppm)
0.0 0.5 1.0
Eff. Cl (apfu)
Eff. Cl (apfu)
eU (ppm)
rmr$_o$
SUPERIOR PROVINCE
SAMPLES NORMALIZED
D.
AFT Age (Ma)
09SZ-23-01
low N, eU,
& eCl
^{238}U (ppm)
Eff. Cl (apfu)
E.
09SRB-M100
Spurious Corr.
eU (ppm)
Eff. Cl (apfu)
F.
14SUB-H43
< eU variability
higher eCl
eU (ppm)
Eff. Cl (apfu)

Figure7

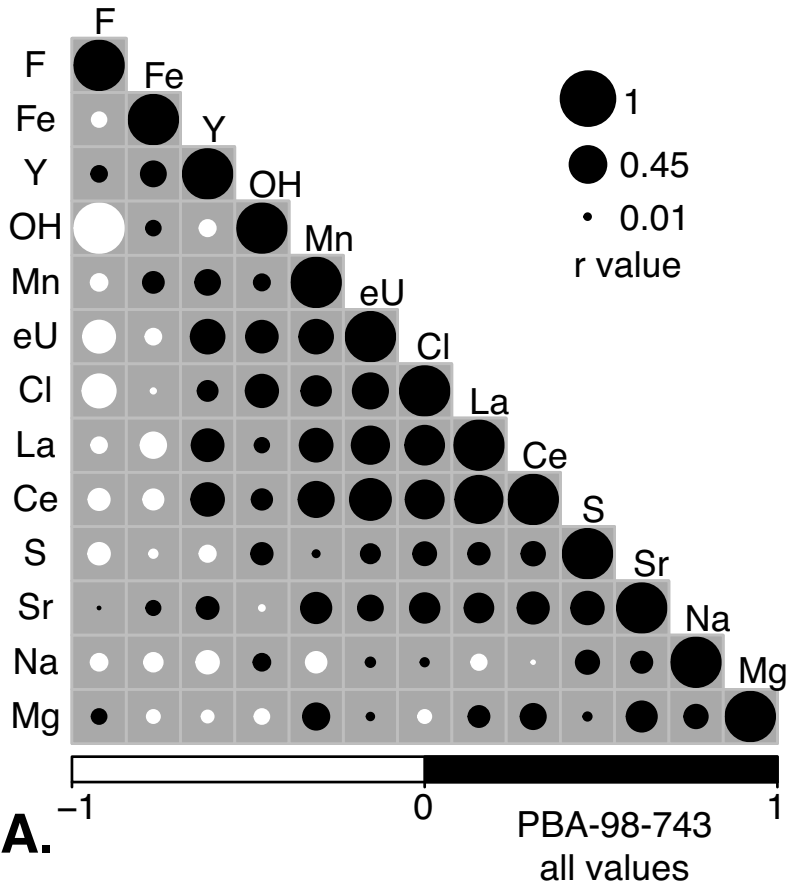
F
Fe
Y
OH
Mn
eU
Cl
La
Ce
S
Sr
Na
Mg
1
0.45
0.01
r value
−1
0
1
PBA-98-743
all values
A.

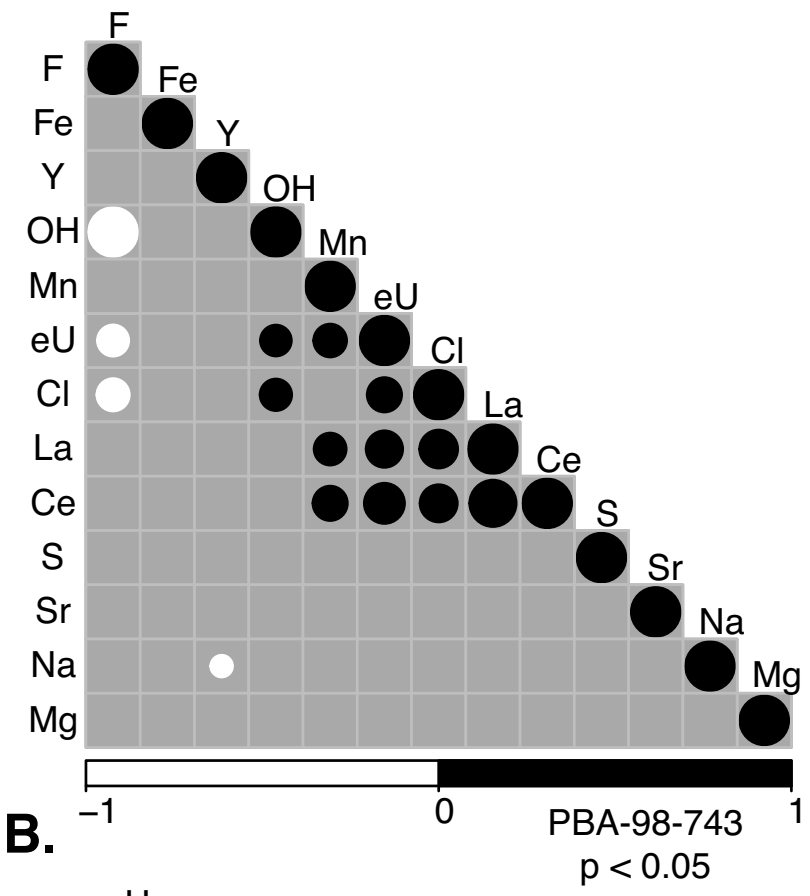
F
Fe
Y
OH
Mn
eU
Cl
La
Ce
S
Sr
Na
Mg
−1
0
1
PBA-98-743
p < 0.05
B.

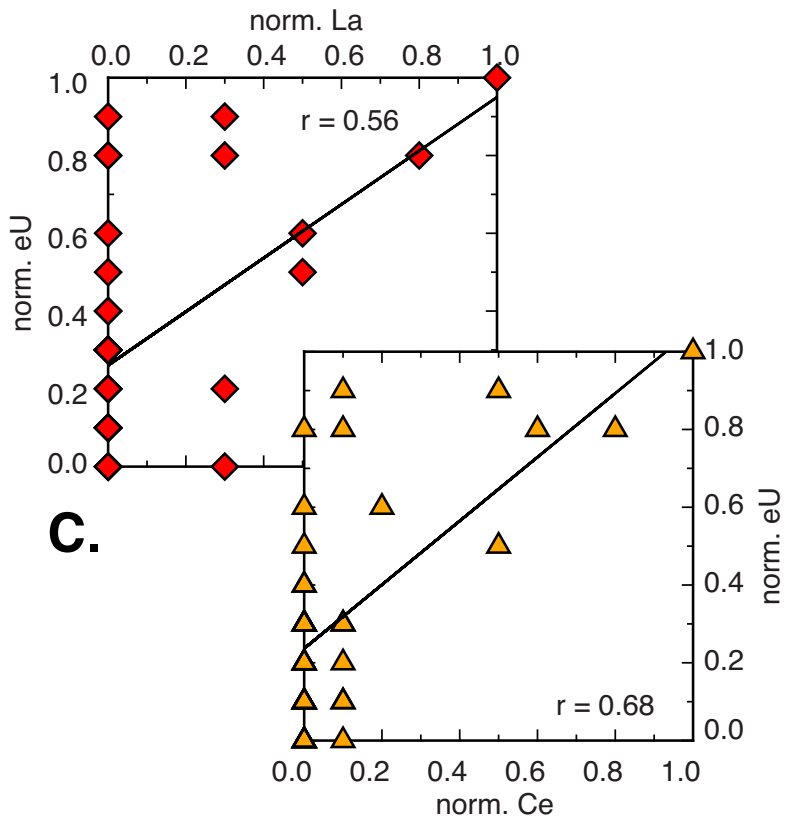
norm. La
norm. eU
r = 0.56
r = 0.68
norm. Ce
C.

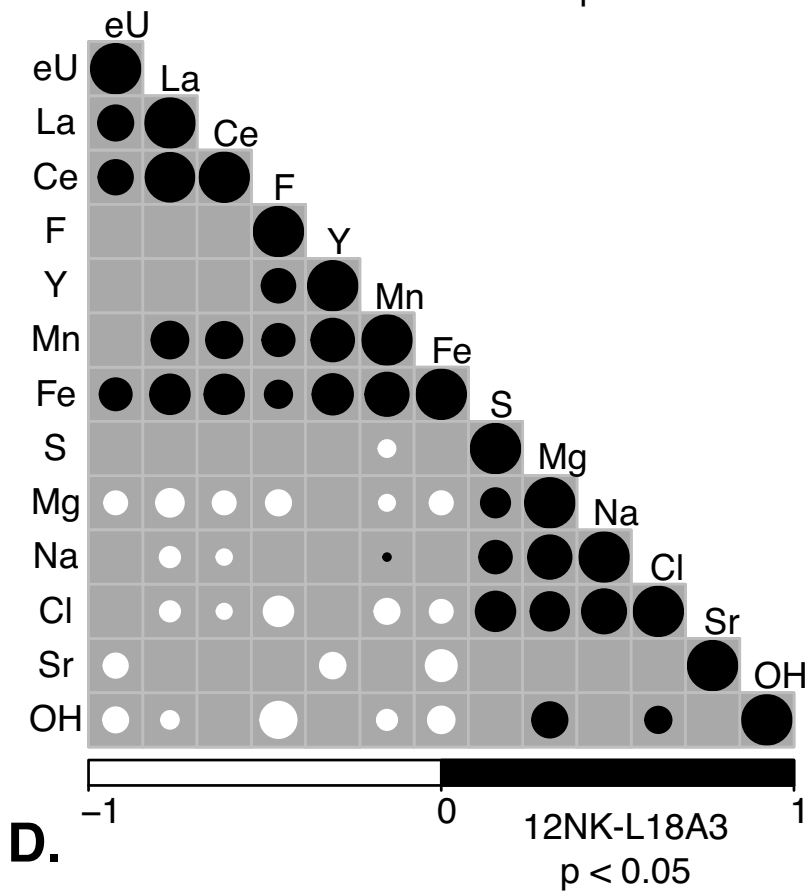
eU
La
Ce
F
Y
Mn
Fe
S
Mg
Na
Cl
Sr
OH
−1
0
1
12NK-L18A3
p < 0.05
D.

Figure8

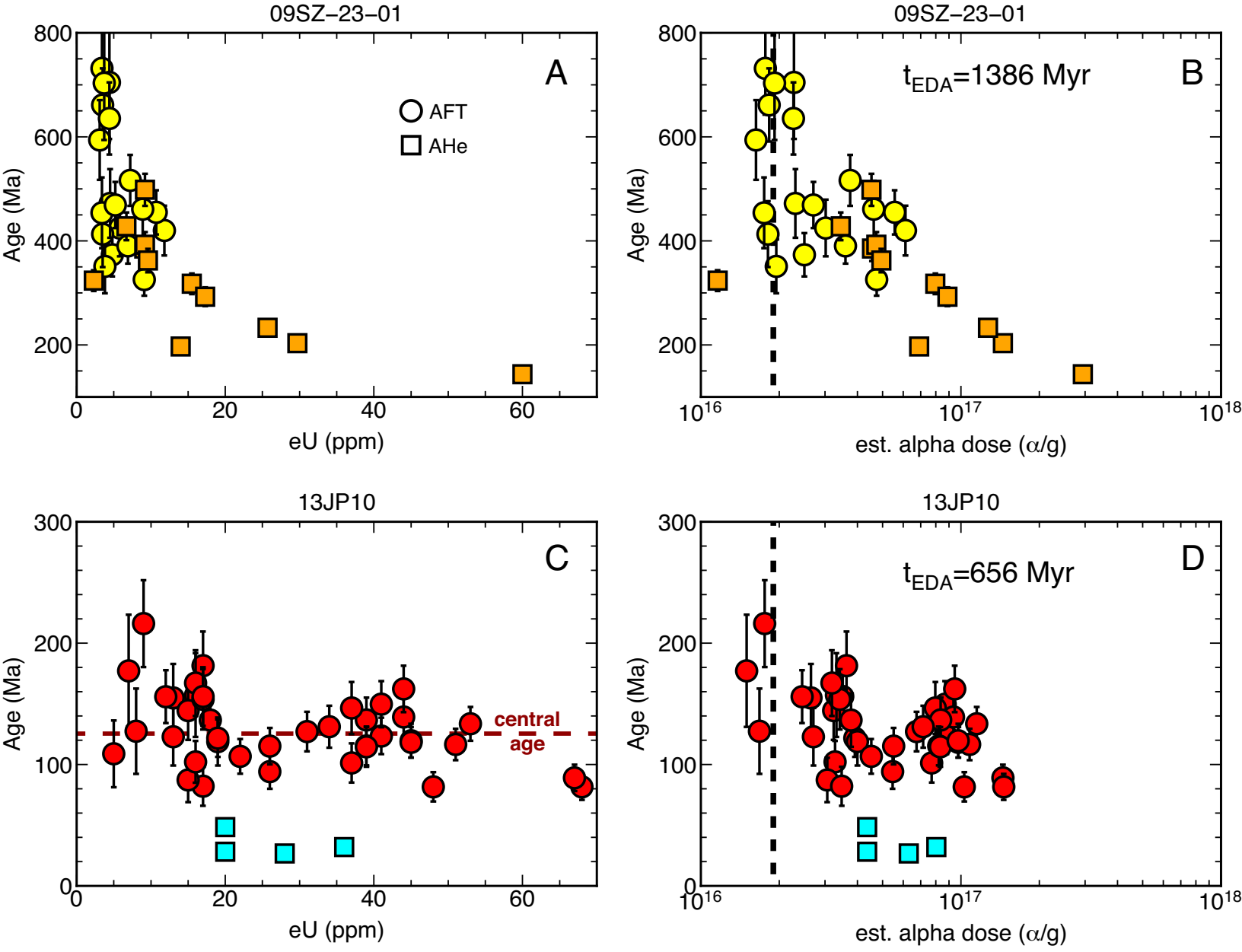
09SZ–23–01
A
AFT
AHe
Age (Ma)
eU (ppm)
09SZ–23–01
B
t_{EDA}=1386 Myr
est. alpha dose (α/g)
13JP10
C
central age
Age (Ma)
eU (ppm)
13JP10
D
t_{EDA}=656 Myr
est. alpha dose (α/g)

Figure9

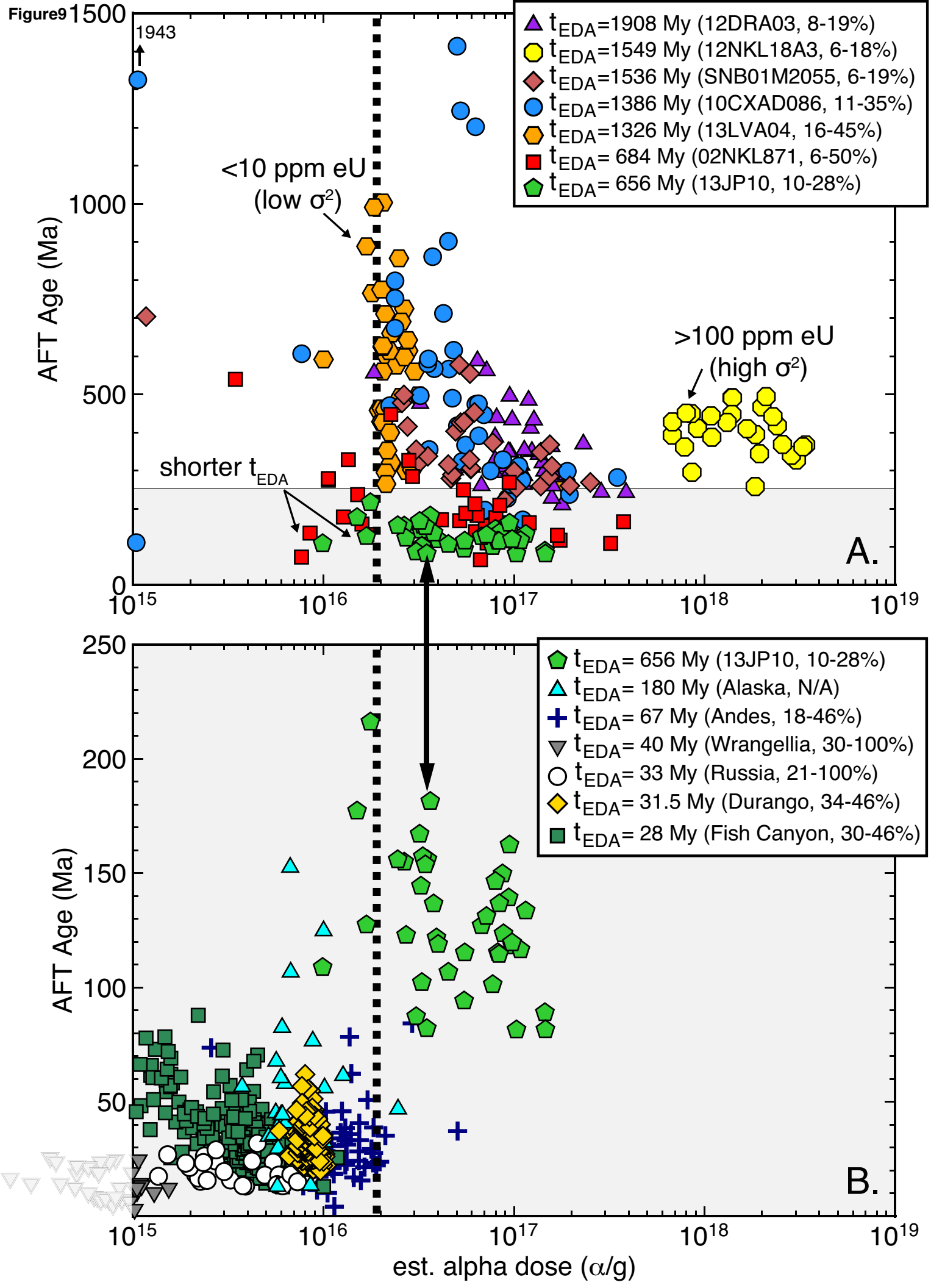
1943
<10 ppm eU
(low σ²)
>100 ppm eU
(high σ²)
shorter t_EDA
t_EDA=1908 My (12DRA03, 8-19%)
t_EDA=1549 My (12NKL18A3, 6-18%)
t_EDA=1536 My (SNB01M2055, 6-19%)
t_EDA=1386 My (10CXAD086, 11-35%)
t_EDA=1326 My (13LVA04, 16-45%)
t_EDA= 684 My (02NKL871, 6-50%)
t_EDA= 656 My (13JP10, 10-28%)
A.
AFT Age (Ma)
0
500
1000
1500
10^15
10^16
10^17
10^18
10^19
t_EDA= 656 My (13JP10, 10-28%)
t_EDA= 180 My (Alaska, N/A)
t_EDA= 67 My (Andes, 18-46%)
t_EDA= 40 My (Wrangellia, 30-100%)
t_EDA= 33 My (Russia, 21-100%)
t_EDA= 31.5 My (Durango, 34-46%)
t_EDA= 28 My (Fish Canyon, 30-46%)
B.
AFT Age (Ma)
50
100
150
200
250
10^15
10^16
10^17
10^18
10^19
est. alpha dose (α/g)

Figure10

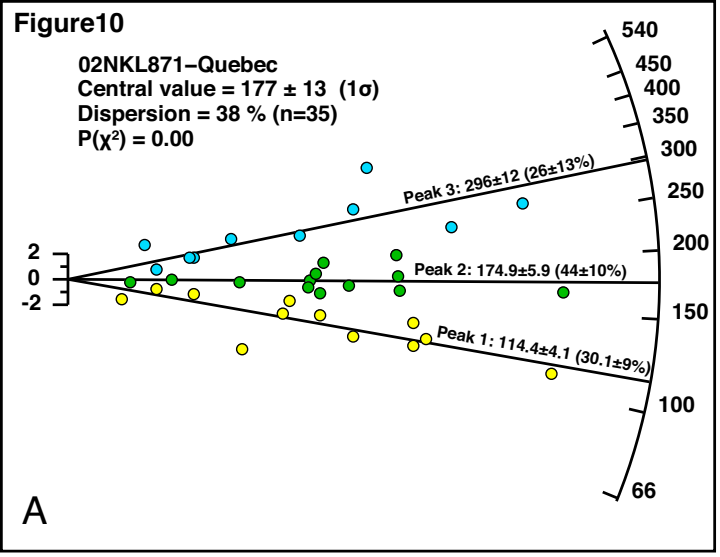
02NKL871–Quebec
Central value = 177 ± 13 (1σ)
Dispersion = 38 % (n=35)
P(χ²) = 0.00
Peak 3: 296±12 (26±13%)
Peak 2: 174.9±5.9 (44±10%)
Peak 1: 114.4±4.1 (30.1±9%)
540
450
400
350
300
250
200
150
100
66
2
0
-2
A

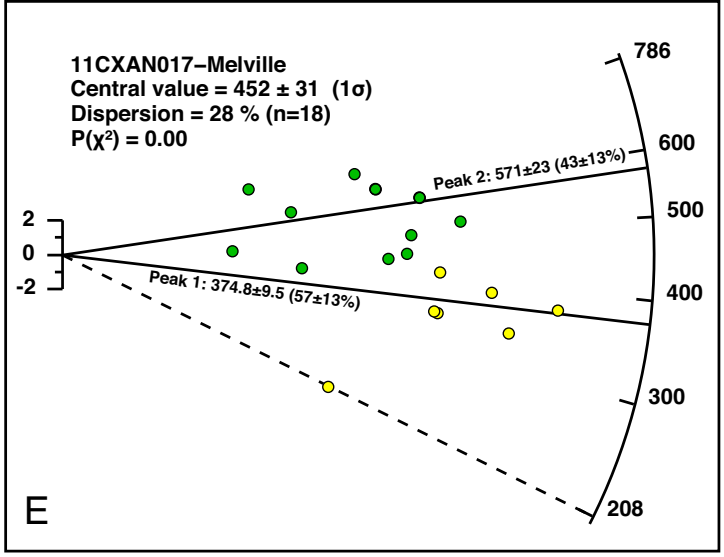
11CXAN017–Melville
Central value = 452 ± 31 (1σ)
Dispersion = 28 % (n=18)
P(χ²) = 0.00
Peak 2: 571±23 (43±13%)
Peak 1: 374.8±9.5 (57±13%)
786
600
500
400
300
208
2
0
-2
E

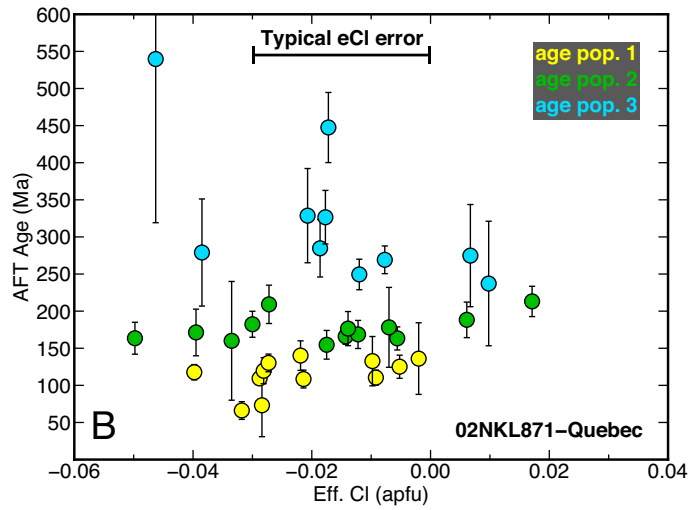
Typical eCl error
age pop. 1
age pop. 2
age pop. 3
AFT Age (Ma)
Eff. Cl (apfu)
B
02NKL871–Quebec

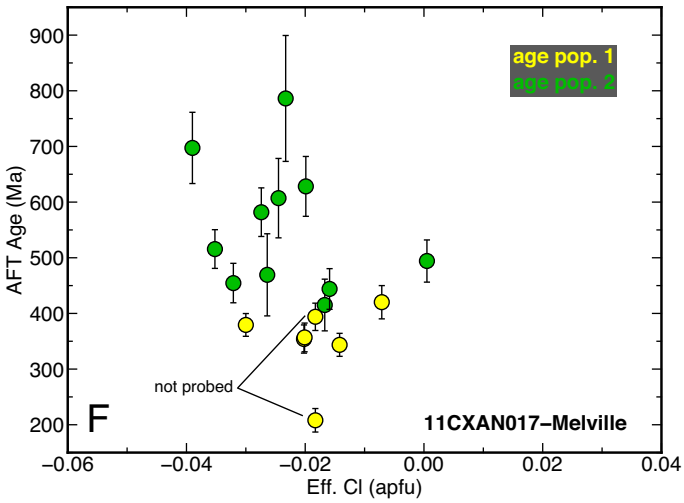
age pop. 1
age pop. 2
not probed
AFT Age (Ma)
Eff. Cl (apfu)
F
11CXAN017–Melville

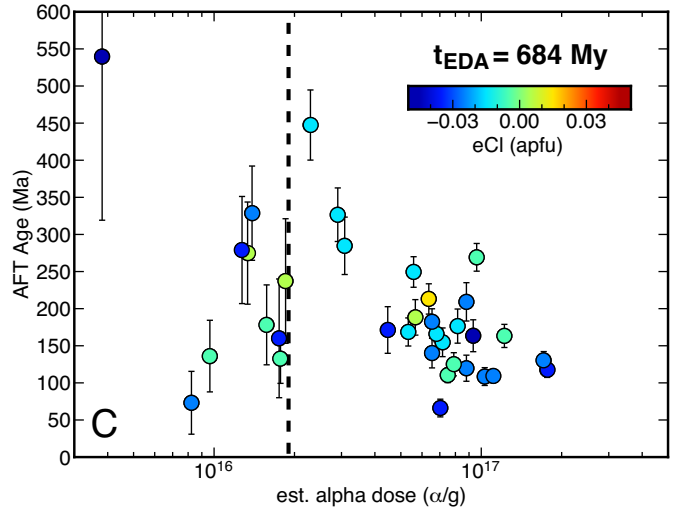
t_EDA = 684 My
−0.03 0.00 0.03
eCl (apfu)
AFT Age (Ma)
est. alpha dose (α/g)
C

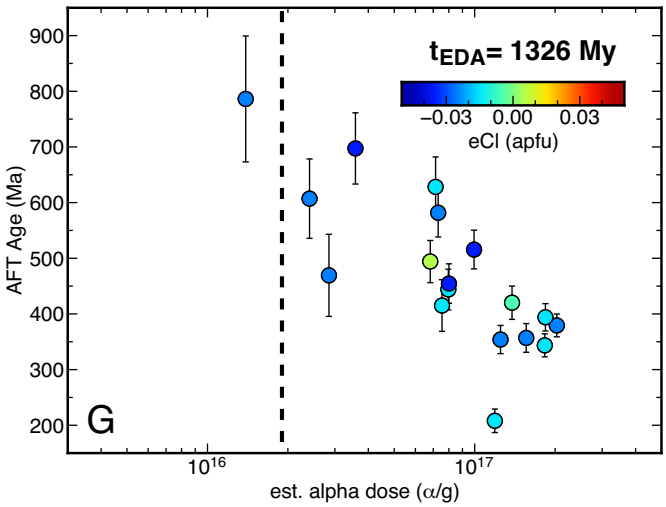
t_EDA = 1326 My
−0.03 0.00 0.03
eCl (apfu)
AFT Age (Ma)
est. alpha dose (α/g)
G

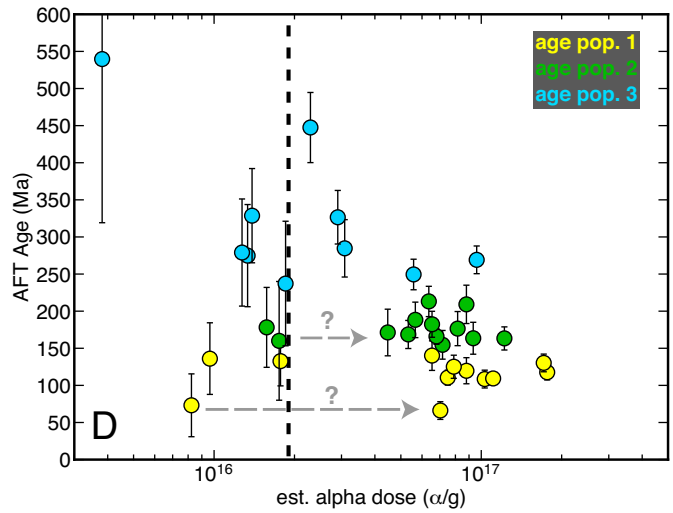
age pop. 1
age pop. 2
age pop. 3
?
?
AFT Age (Ma)
est. alpha dose (α/g)
D

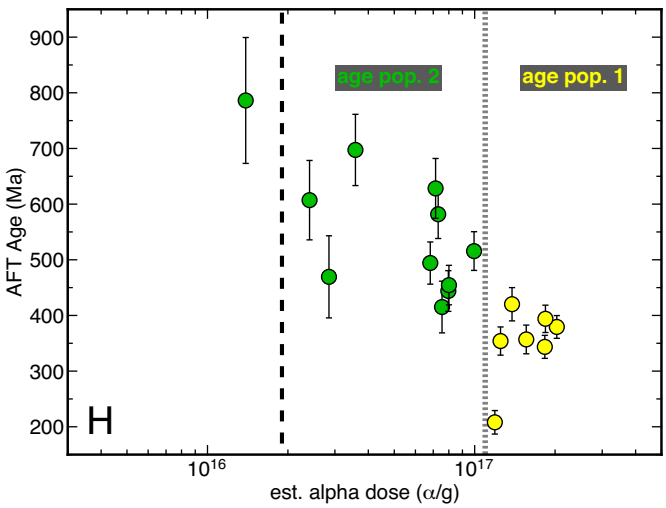
age pop. 2
age pop. 1
AFT Age (Ma)
est. alpha dose (α/g)
H